Science and Technology for the Built Environment, (2026) **32**, 206–225

ISSN: 2374-4731 print / 2374-474X online
DOI: 10.1080/23744731.2025.2582421

Integration of a thermal aerosol generator into a full-scale HVAC filter test rig for aging filters with representative urban aerosol size distributions (RP-1734)

CHUNXU HUANG and BRANDON E. BOOR*

Lyles School of Civil and Construction Engineering, Purdue University, West Lafayette, IN, USA

HVAC filter performance is significantly influenced by the physicochemical properties of the aerosol the filters encounter. HVAC filters play a critical role in maintaining indoor air quality by removing airborne particles, making it essential to accurately simulate real-world filtration conditions during standardized testing. Among aerosol properties, the particle size distribution (PSD) is a key factor governing filter loading behavior and efficiency. However, current standardized protocols rely primarily on coarse-mode loading dusts that poorly represent the submicrometer number and mass PSDs characteristic of urban atmospheric aerosol. The overarching goal of ASHRAE RP-1734 is to develop a novel methodology for rapidly aging HVAC filters by simulating their pressure drop evolution over their service life, enabling more accurate assessments of blower energy consumption and informing optimal filter replacement schedules. As part of this effort, the present study evaluates the integration of a thermal aerosol generator (TAG) with a full-scale HVAC filter test rig and assesses its suitability for filter loading applications. Controlled experiments were conducted to characterize in-duct number and mass PSDs under varying operational conditions, including volumetric airflow rate, relative humidity, and salt stick feed rate. The TAG-generated aerosol exhibited a stable unimodal distribution, with a submicrometer peak near 100 nm in the number PSD and 150 nm in the mass PSD, with only minor shifts in modal diameter across operational conditions. Notably, the number PSDs closely aligned with those observed in urban environments. Although the mass PSDs differed by approximately 100 nm from typical urban aerosol mass PSDs, they still effectively captured the submicrometer fraction, especially when compared to standardized coarse-mode loading dusts. This study demonstrates the TAG's ability to generate stable, reproducible PSDs across diverse conditions, enabling realistic simulation of urban aerosol properties in a controlled laboratory setting. Incorporating TAG-generated aerosol into standardized HVAC filter testing protocols offers a more representative approach to evaluating filter performance and informs the design of filters that enhance indoor air quality in urban environments.

Introduction

Aerosol physicochemical properties and HVAC filter performance evaluation

The adverse effects of poor indoor air quality on human health and well-being are well documented (Brook et al. 2010; Kamaruzzaman and Sabrani 2011; Tham 2016; Van Tran, Park, and Lee 2020; Deng et al. 2024). Indoor air quality is shaped by both the transport of outdoor particles into buildings and emissions from indoor sources, each contributing to elevated particle concentrations in occupied environments. Outdoor particles are transported into the indoor environment via mechanical ventilation through HVAC systems, natural ventilation through open windows and doors, and infiltration through cracks and gaps in the building envelope. HVAC filters play a critical role in cleaning mechanically ventilated outdoor air, thereby reducing occupant exposure to particles of outdoor origin. In commercial buildings, where large volumes of outdoor air are continuously introduced to meet ventilation requirements, inadequate filtration can lead to elevated exposure to outdoor particles.

Indoors, submicrometer particles are generated from various sources, including cooking (Jiang et al. 2021a), combustion (Patra et al. 2024a), cleaning product use (Jiang et al. 2021b), personal care product use (Jiang et al. 2023; Liu et al. 2025), and secondary organic aerosol formation from terpene and skin oil ozonolysis (Rosales et al. 2022; Liu et al. 2024; Patra et al.

Received January 7, 2025; accepted October 1, 2025
Chunxu Huang, Student Member ASHRAE, is a PhD student. **Brandon E. Boor, PhD**, is the Dr. Margery E. Hoffman Associate Professor.
Supplemental data for this article can be accessed online at https://doi.org/10.1080/23744731.2025.2582421.
*Corresponding author e-mail: bboor@purdue.edu

2024b). Human occupants contribute further to indoor particle levels through emissions from skin, clothing, and exhaled breath (Patra et al. 2021). As over 55% of the global population now resides in urban areas, a proportion expected to reach 68% by 2050 (United Nations 2018), inhalation exposure to urban aerosol has become an increasingly important public health concern, contributing to cardiovascular and respiratory diseases, asthma, neurological disorders, and elevated rates of morbidity and mortality (Wu and Boor 2021). Effective air filtration is therefore essential for reducing particle exposures, particularly in densely occupied commercial buildings in urban areas, where high outdoor air ventilation rates and occupant density amplify exposure risks.

The classical theory of particle deposition onto filter fibers identifies five fundamental removal mechanisms: interception, inertial impaction, diffusion, gravitational settling, and electrostatic attraction (Hinds and Zhu 2022). The interaction between particles and filter fibers is governed by the physicochemical properties of the aerosol population, which in turn affects both removal efficiency and filter loading behavior. Key aerosol properties, including the particle size distribution (PSD), dynamic shape factor, and effective density, determine how particles navigate airflow and interact with fibers. Chemical composition affects adhesion and the potential for agglomeration or chemical reactions, while phase state (solid, semisolid, liquid) governs deposition behavior upon contact (Tumminello et al. 2021; 2024). Hygroscopicity, or the ability to absorb moisture, alters particle size and mass, impacting deposition dynamics in humid environments. Additionally, electrostatic charges on particles enhance deposition by attracting them to fibers or previously deposited particles (Pöschl 2005; Huang et al. 2025).

The PSD is critical for characterizing aerosol dynamics and significantly influences filtration efficiency and the filter loading process, alongside factors such as air velocity and filter fiber diameter (Hinds and Zhu 2022; Berry et al. 2023). Experimental studies have demonstrated that the mass ratio of fine ($\leq$1000 nm) to coarse (>1000 nm) particles in bimodal aerosol strongly affects filter performance, including pressure drop and removal efficiency. Poon and Liu (Poon and Liu 1997a, 1997b) found that higher ratios of fine particles accelerated increases in pressure drop across filters. Similarly Lee et al. (Lee et al. 2001) observed that filters exposed to more coarse-mode particles exhibited slower increases in pressure drop, as dense cakes formed by fine particles more effectively restricted airflow. Giffin et al. (Giffin et al. 2012) confirmed the influence of aerosol PSDs on HEPA filter loading curves, and Wang et al. (Wang et al. 2016) demonstrated that fine particles enhance depth filtration, forming denser surface dust cakes. In contrast, Valmari et al. (Valmari et al. 2006) reported greater pressure drops with coarse particles alone compared to mixtures of fine and coarse particles. Collectively, these findings underscore the importance of PSDs in affecting filter behavior. Theoretical models, such as those developed by Endo et al. (Endo et al. 1998a; 1998b), predict pressure drops based on dust cake porosity and particle morphology and were validated by Kim et al. (Kim et al. 2009). Tian et al. (Tian et al. 2019) further emphasized that increased fine particle fractions raise filter pressure drop and reduce dust holding capacity, reinforcing the importance of aerosol PSDs in influencing filter performance.

Standardized testing of HVAC filters and real-world discrepancies

Despite extensive research on filter loading, most studies have focused on flat sheet filter media and evaluated only a limited portion of the filter lifespan. Comprehensive studies on full-scale HVAC filters used in commercial buildings throughout their entire lifecycle remain scarce, primarily due to the high costs involved. Constructing a full-scale test rig to accommodate HVAC filters and replicate real-world conditions is both labor-intensive and expensive. The frequent replacement of HVAC filters and the lack of techniques to generate high mass concentration loading dusts at elevated volumetric airflow rates further complicate such studies (Arunkumar et al. 2007). To address these challenges, many studies have evaluated in situ filter performance within real-world building HVAC systems, utilizing natural ambient aerosol as the loading medium to reduce costs and avoid constructing new test rigs. Numerous in situ studies have measured filtration efficiencies in residential and commercial buildings, comparing results with laboratory data provided by standards or manufacturers. These in situ measurements often differ from laboratory results, underscoring the need to revise laboratory testing protocols to better reflect real-world performance.

Raynor and Soo (2003) found that charge decay during service led to discrepancies between electret filter performance in real HVAC systems and standardized tests, prompting revisions to testing protocols. Numerous studies have examined how dust loading affects HVAC filter performance and system energy consumption. Zaatari et al. (Zaatari et al. 2014) analyzed rooftop units, finding that dust loading significantly influences efficiency and energy consumption, with efficiency increasing for uncharged filters. Li and Siegel (2020b) observed similar trends. They also compared in situ results with laboratory data, advocating for more realistic laboratory tests with indoor-like aerosol (Li and Siegel 2020a). Alavy et al. analyzed the energy penalties associated with filter pressure drop, demonstrating that the impact of high-efficiency filters on energy consumption is highly dependent on system-specific factors, such as HVAC runtime and fan motor type (Alavy and Siegel 2019; Alavy et al. 2020). Their findings indicate that in residential systems with low HVAC runtime, the energy implications of using higher efficiency filters are minimal, whereas in commercial systems with extended runtimes, these impacts become more pronounced. Moreover, energy consumption increases with higher filter pressure drop in speed-controlled fans but decreases in systems lacking speed control. These observations align with earlier studies (First et al. 1992; Stephens et al. 2010; Zaatari et al. 2014). Importantly, the authors emphasize the need to account for filter loading over a filter's service life, noting significant discrepancies between laboratory and in situ performance due to the use of unrealistic test dusts. This highlights the importance of

developing improved laboratory testing protocols that incorporate more representative loading aerosol.

While in situ loading offers the most realistic evaluation of HVAC filters by using real-world conditions, it is also time-consuming and labor-intensive due to extended loading periods and instrument maintenance. Laboratory-based testing, in contrast, provides a standardized and repeatable method for assessing HVAC filter performance, enabling accelerated and consistent evaluations across various filter designs. Current standards for full-scale HVAC filter testing include ANSI/ASHRAE Standard 52.2-2017 (ASHRAE 2017) in the United States, ISO 16890-1:2016 (introduced to replace European Standard EN 779), and Chinese National Standard GB/T 14295. These standards primarily target sub-HEPA efficiency filters and incorporate dust holding capacity into their procedures, recognizing the impact of dust loading on filtration efficiency. However, those standards utilize test dusts with particle sizes larger than those typically found in urban environments, resulting in limited applicability for realistic filter lifetime modeling. These standardized loading dusts are widely used in both industry and research for full-scale HVAC filter testing (Hanley et al. 1994; 1999; Raynor and Soo 2003; Giffin et al. 2012; Knobloch et al. 2024).

A defining characteristic of standardized loading test dusts, such as ASHRAE and ISO 12103-1 test dusts, is their dominance by coarse-mode particles (Tronville and Rivers 2005). Although the carbon black fraction in ASHRAE test dust was intended to represent submicrometer particles, electrostatic interactions and cohesive forces within dust feeder systems promote agglomeration, resulting in an in-duct PSD that is significantly larger than the nominal composition of the dust. Moreover, present-day urban outdoor air contains significantly fewer coarse particles than when ASHRAE test dust was originally formulated, primarily due to advances in pollution control technologies and regulatory interventions. This shift in ambient aerosol characteristics underscores the need for finer, more representative loading dusts in HVAC filter testing protocols. However, coarse particles offer advantages in experimental efficiency and reproducibility. Their high mass loading rates enable accelerated testing, significantly reducing evaluation time. Additionally, these standardized test dusts are commercially available and reliably consistent, ensuring reproducibility and comparability across studies. Despite these benefits, coarse-mode particles poorly represent submicrometer aerosol modes, including the accumulation mode (100 to 1000 nm), Aitken mode (10 to 100 nm), and nucleation mode ($\leq$ 10 nm). The accumulation mode contributes substantially to urban mass PSDs, while Aitken and nucleation modes dominate urban number PSDs (Wu and Boor 2021). Consequently, relying solely on coarse-mode aerosol in HVAC filter loading tests may bias performance evaluations. Coarse particles primarily promote surface filtration, whereas submicrometer particles are more likely to penetrate and engage in depth filtration within the filter media. The absence of submicrometer particles in standardized tests may lead to incomplete or misleading assessments of HVAC filter performance under real-world conditions.

Advancements in submicrometer aerosol generation for HVAC filter testing

The development of more representative loading aerosol with PSDs that accurately reflect atmospheric conditions is essential for standardizing laboratory HVAC loading tests and improving their relevance to urban environments. To effectively simulate full-scale HVAC filter loading behavior, the loading aerosol must not only replicate atmospheric PSDs but also reach sufficiently high concentrations to enable rapid and consistent filter loading under elevated volumetric airflow rates. While submicrometer particle generation techniques exist, they often suffer from low mass production rates (Biskos et al. 2008), limiting their applicability. ANSI/ASHRAE Standard 52.2-2017 Appendix J prescribes the use of atomized potassium chloride (KCl) aerosol from an aqueous solution to condition electret filters, aiming to simulate temporal charge decay observed in real-world applications (ASHRAE 2017). While suitable for evaluating electret charge stability, this conditioning process is not intended for HVAC filter loading assessments. The Appendix J aerosol, with a count median diameter (CMD) of approximately 40 to 50 nm and a number concentration below $1 \times 10^6\,\mathrm{cm}^{-3}$, is suboptimal for rapid filter loading evaluations due to its limited mass loading potential. For more representative assessments of the impact of HVAC filter clogging on blower energy consumption during rapid aging experiments, it is essential to use finer PSDs reflective of urban atmospheric conditions and to achieve higher aerosol concentrations.

Thermal aerosol generation offers a promising alternative to the Appendix J aerosol (Zhang and Jiang 2016), producing high mass concentrations of submicrometer salt particles through the evaporation-condensation of salt vapor. However, its potential for evaluating filter loading performance remains largely unexplored. A thermal aerosol generator (TAG) has demonstrated the capability to produce submicrometer mass PSDs with shapes similar to those observed in urban outdoor air. The properties and performance of synthetic submicrometer salt aerosol generated by the TAG were comprehensively evaluated in a previous study (Wu and Boor 2020), providing a strong foundation for their use in standardized HVAC filter loading tests. This approach offers a practical solution to bridge the gap between laboratory testing and real-world filter performance, enhancing the accuracy and relevance of HVAC filter evaluation protocols.

The overarching goal of ASHRAE RP-1734 is to develop a novel methodology for rapidly aging HVAC filters by simulating their pressure drop evolution over their service life, enabling more accurate assessments of blower energy consumption and informing optimal filter replacement schedules. As part of this effort, the present study evaluates the integration of a TAG with a custom-designed full-scale HVAC filter test rig and assesses its suitability for accelerated filter loading. This includes detailed characterization of in-duct number and mass PSDs under varying operational conditions. Measuring in-duct PSDs is essential, as conventional ASHRAE test dust tends to shift toward coarser size distributions during dispersion into the test rig. In addition, key test rig parameters, such as the volumetric airflow rate, relative humidity (RH), and the spatial uniformity of the aerosol concentration and air velocity across the filter face,

are characterized. These parameters are critical for validating the feasibility of synthetic aerosol-based rapid loading protocols in support of the forthcoming ASHRAE Guideline 35, *Method for Determining the Energy Consumption Caused by Air-Cleaning and Filtration Devices*, which seeks to establish standardized methods for determining the energy use of air-cleaning and filtration systems.

Materials and methods

Description of the thermal aerosol generator

The experimental setup features a TAG (Type 6000, SFP Services Ltd., Christchurch, UK) designed to produce high mass concentrations of submicrometer salt aerosol (Figure 1). This device operates using a high-temperature oxygen (O_2)–propane (C_3H_8) flame for aerosol generation. The TAG generates two types of salt aerosol: KCl and sodium chloride (NaCl). Cylindrical salt sticks (SFP Services Ltd., Christchurch, UK) are manufactured with a small quantity of magnesium oxide (MgO) as a binding agent to ensure structural integrity. In this study, KCl was selected as the aerosol material due to its lower corrosivity compared to NaCl, as well as its higher deliquescence point than that of NaCl (Wise et al. 2007; Freney et al. 2009). The cylindrical salt sticks, measuring 10 mm in diameter and 100 mm in length, had an effective salt density ranging from 0.1 to 0.13 g mm^{-1}. Approximately 13% of the stick's original weight, comprising MgO used as a binding agent, remains as nonvaporized hot ash during the process.

The TAG consists of two primary functional components: the salt stick feeding mechanism and the O_2–C_3H_8 flame combustion system (Figure 1). The feeding mechanism employs a drive roller and a sprung guide arm-connected smooth idler roller to securely mount and propel the salt stick. A variable-speed motor, powered by a built-in battery and connected via a gearbox, controls the drive roller's rotation, enabling precise stick feeding through a nozzle into the flame burner. The flame burner comprises a blowtorch and two gas flow meters that regulate O_2 and C_3H_8 flow rates, nominally set at 17 L min^{-1} and 4 L min^{-1}, respectively. Upon ignition, the mixed gases produce an annular flame cone that surrounds the salt stick. This high-temperature environment vaporizes the salt, which then condenses into submicrometer aerosol with a high mass concentration.

Integration of the TAG with a full-scale HVAC filter test rig

A full-scale HVAC duct system was constructed as the test rig for evaluating commercial HVAC air filters using synthetic submicrometer aerosol generated by the TAG (Figure 2). The ductwork measures 28 ft (8.5 m) in length with a cross-sectional area of 2 × 2 ft (610 × 610 mm) and is constructed from 22-gauge galvanized steel sheets. The interior surface is smooth, and the structure is rigid, maintaining its form under the specified operating pressures. The TAG is strategically positioned atop the test rig to allow for easy access during salt stick replacement and routine maintenance. Salt aerosol is drawn through an insulated 90° injection elbow with a 10 × 10 inch (254 × 254 mm) square cross section. The injection elbow is equipped with an adjustable damper to regulate the aerosol intake volume. The TAG is positioned at a fixed distance from the injection elbow, ensuring that the flame cone's tip partially enters the elbow inlet for optimal aerosol capture. This setup also provides sufficient clearance for operational adjustments and observation.

A MERV 8 filter was installed at the air intake of the test rig to remove coarse particles, followed by a flow straightener to ensure uniform airflow. A large-scale steam humidifier, capable of producing up to 30 lb h^{-1} of steam, was positioned near the air intake. The steam humidifier injection tube was placed between the MERV 8 intake filter and the flow straightener, allowing for the mixing of intake air, moisture, and salt aerosol flow after passing through the 90° elbow. The aerosol-laden airflow then challenged the downstream test filter housed in a custom-designed filter bank, capable of accommodating various filter configurations. Three MERV-rated filters—MERV 8, MERV 13, and MERV 14—were selected as test filters, in accordance with the requirements of ASHRAE RP-1734 (Supplementary Table S1).

A high-capacity tubular inline centrifugal blower (Model TSL122, Twin City Fans & Blowers, Plymouth, MN, USA) was installed at the end of the test rig to draw in laboratory air. This setup created a negative pressure environment,

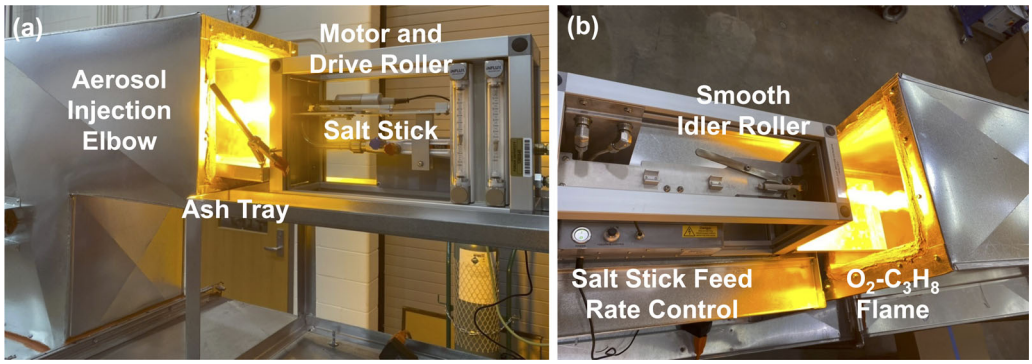

Fig. 1. Photographs of the thermal aerosol generator: (a) side view and (b) top view.

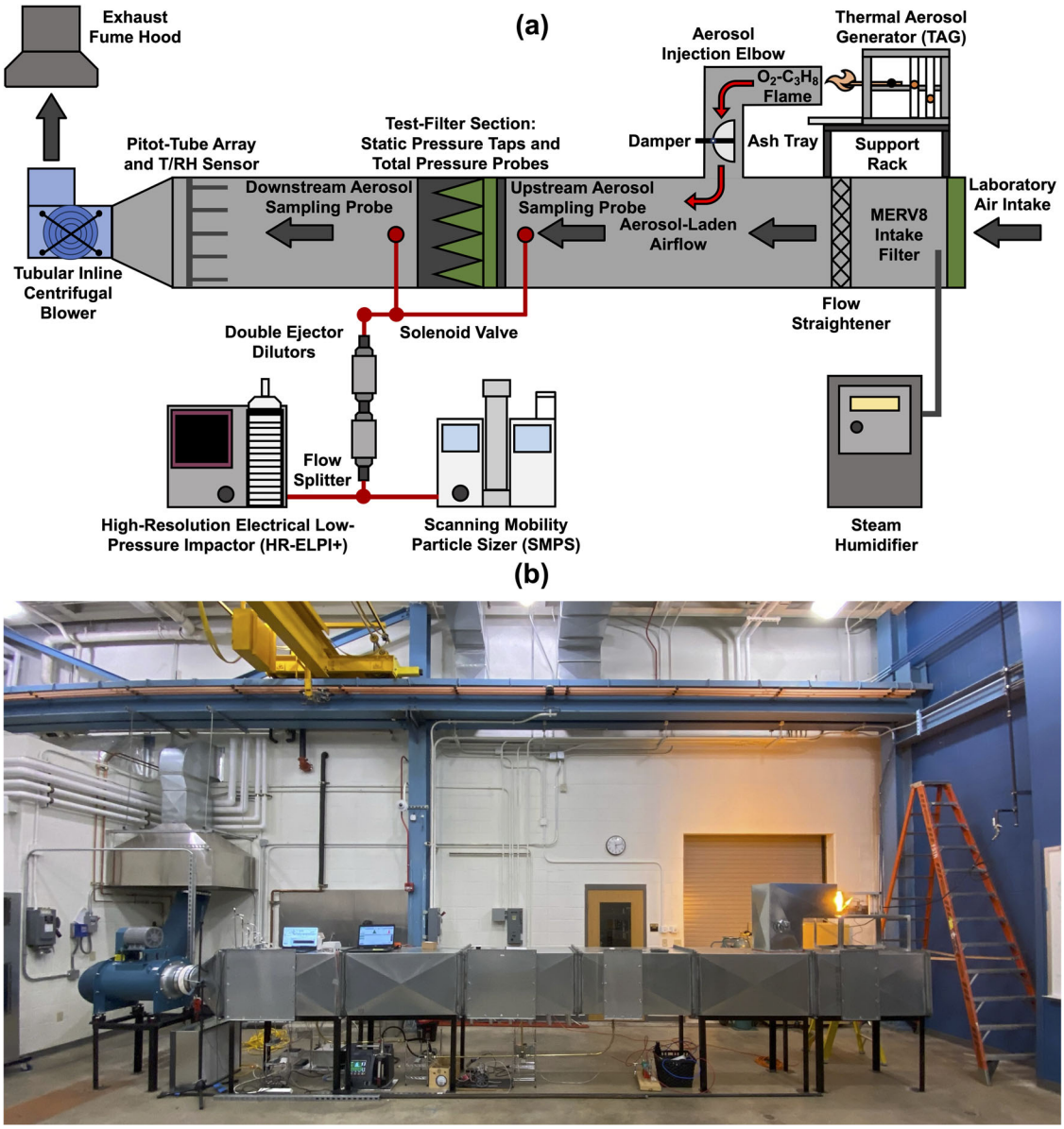

Fig. 2. Full-scale HVAC filter test rig: (a) schematic diagram and (b) photograph of the experimental setup.

facilitating the introduction of TAG-generated aerosol and ensuring thorough mixing within the system. To prevent residual aerosol from recirculating into the laboratory or test rig, an exhaust fume hood was positioned downstream of the blower to safely expel remaining salt aerosol into the outdoor atmosphere.

Experimental design

Before aging experiments commenced, the test filters were weighed to determine their initial mass. These preloading measurements were recorded prior to installation in the test rig. Once the in-duct airflow and RH were stabilized, the TAG was ignited to generate KCl aerosol, initiating the aging process. To maintain continuous filter aging, salt sticks were periodically replaced as they were consumed. During these replacement procedures, transient shifts toward smaller PSDs were observed, attributed to the finer size characteristics of flame-generated aerosol compared to the KCl aerosol. However, the use of standardized salt sticks from the same manufacturing lot ensured consistent KCl aerosol production, rendering these temporary PSD fluctuations negligible within the context of the experimental protocol. The experimental process continued until the final pressure drop (ΔP) across the test filter reached 1.5 in H_2O. During loading, safety and maintenance parameters, including gas cylinder pressure and ambient combustion gas levels for leak detection, were monitored and recorded, along with the timing of salt stick replacements.

Sensitivity experiments were conducted to evaluate filter aging behavior and performance under different operating conditions. Each filter type was subjected to four test categories: (1) baseline test, (2) volumetric airflow rate sensitivity, (3) salt stick feed rate sensitivity, and (4) RH sensitivity.

For each category, three to five replicate experiments were performed to ensure repeatability. The specific loading conditions for each test category are summarized in Table 1.

Instrumentation and operational control

The in-duct aerosol number concentrations and size distributions from 6 to 1000 nm (0.006 to 1 μm) were measured in real-time using two instruments: (1) a scanning mobility particle sizer (SMPS) (Model 3938NL88, TSI, Inc., Shoreview, MN, USA) with a long differential mobility analyzer (DMA) and (2) a high-resolution electrical low-pressure impactor (HR-ELPI+) (Dekati Ltd., Kangasala, Finland) equipped with oil-soaked sintered collection plates. The SMPS provides number PSDs based on electrical mobility diameter (D_{em}), while the HR-ELPI+ offers aerodynamic diameter (D_a)-based number PSDs. The SMPS system includes a Kr-85 bipolar charger, long DMA, and a water-based condensation particle counter (CPC) (Model 3788, TSI, Inc., Shoreview, MN, USA). Particles are initially charged to a known distribution using the bipolar charger, classified by an electric field in the DMA, and counted by the CPC through optical detection. The SMPS measured particles from D_{em} = 20.1 to 1000 nm with a 4-min scan duration. Data analysis utilized number PSDs ($dN/dLogD_{em}$; cm^{-3}) directly extracted using the Aerosol Instrument Manager (AIM) software (TSI, Inc., Shoreview, MN, USA). The HR-ELPI+ uses a unipolar charger to charge particles before classifying them by inertial impaction through a cascade impactor. Charged particles are detected upon impact on sintered collection plates using sensitive electrometers. Operating at a 1-Hz sampling rate, the HR-ELPI+ measures number PSDs ($dN/dLogD_a$; cm^{-3}) from D_a = 6 to 10,000 nm, enabling real-time monitoring of the KCl loading aerosol. Deviations in PSDs detected by the HR-ELPI+ provided immediate indicators of potential TAG issues, such as salt stick feed blockages, stick depletion, or fluctuations in O_2 and/or C_3H_8 flow rates due to compressed gas cylinder depletion.

Aerosol sampling probes were positioned upstream and downstream of the test filter in the test rig to measure TAG-generated KCl aerosol PSDs. The upstream probe was located 1 ft from the filter, while the downstream probe was 12 ft away to promote aerosol mixing and help ensure a uniform distribution downstream. Both probes were centrally positioned to capture representative cross-sectional concentrations. A solenoid valve alternated sampling between the two points. High aerosol concentrations were diluted using a double dilutor system with two series-connected ejector dilutors (DI-1000, Dekati Ltd., Kangasala, Finland), achieving a high dilution factor (DF). The diluted samples were directed into a four-way flow splitter (Model 1104, Brechtel Manufacturing, Inc., Hayward, CA, USA), with two outlets connected to the SMPS and HR-ELPI+ and two open to ambient air to maintain pressure consistency between the intake and outlet. Digital pressure transducers (Series 265, Setra Systems, Inc., Boxborough, MA, USA) monitored pressure differentials across each dilutor to calculate dilution factors based on manufacturer calibration curves.

A pitot-tube array was installed upstream of the inline centrifugal blower to measure the volumetric airflow rate. The array, capable of self-averaging, consisted of five pitot-tubes connected in parallel. An in-duct temperature and RH sensor (Model SRH200, Setra Systems, Inc., Boxborough, MA, USA) was positioned behind the pitot-tube array. Additionally, a barometric pressure sensor (Model 276, Setra

Table 1. Aging conditions for test filters in the ASHRAE RP-1734 baseline and sensitivity tests.

Experiment type	Volumetric airflow rate [ft^3 min^{-1}]	RH [%]	Salt stick feed rate [mm min^{-1}]	Number of experiments per filter type	Filter type
Baseline experiments	2000	42.5 ± 2.5	10	5	MERV 14 MERV 13 MERV 8
Volumetric airflow rate sensitivity experiments	1000	42.5 ± 2.5	10	3	MERV 14 MERV 13 MERV 8
	500			3	MERV 14 MERV 13 MERV 8
Salt stick feed rate sensitivity experiments	2000	42.5 ± 2.5	18	3	MERV 14 MERV 13 MERV 8
			5	3	MERV 14 MERV 13 MERV 8
RH sensitivity experiments	2000	27.5 ± 2.5	10	3	MERV 14
		57.5 ± 2.5		3	MERV 14 MERV 13 MERV 8

Systems, Inc., Boxborough, MA, USA) was installed to measure atmospheric pressure. Using temperature and atmospheric pressure readings, real-time air density was calculated and applied in conjunction with velocity pressure readings from the pitot-tube array to determine real-time in-duct volumetric airflow rates.

All pressure transducers and sensors integrated into the test rig converted physical signals into analog voltage signals, which were processed into numerical data by a data acquisition system. A data acquisition card (Model 6211, National Instruments, Inc., Austin, TX, USA) and LabVIEW software (Version 2020, National Instruments, Inc., Austin, TX, USA) were used to process and record these signals. In addition to data acquisition, the system generated analog voltage signals to control components such as the blower and steam humidifier, enabling precise regulation of operational parameters through proportional–integral–derivative (PID) control algorithms in LabVIEW. This feedback control maintained desired in-duct volumetric airflow rates and RH levels. It also automated the operation of the solenoid valve, alternating aerosol sampling between upstream and downstream of the test filter. Systematic uncertainties, based on manufacturer specifications, are summarized in Table 2.

Analysis of synthetic aging aerosol size distributions

The SMPS and HR-ELPI+ report PSDs as a function of electrical mobility diameter (D_{em}) and aerodynamic diameter (D_a), respectively. PSDs measured by the HR-ELPI+ were used primarily for real-time monitoring and diagnostics of TAG operation, leveraging rapid 1-s sampling intervals. In contrast, the more stable and less fluctuating number PSDs from the SMPS were used for data analysis. Number PSDs ($dN/dLogD_{em}$; cm^{-3}) were converted into surface area ($dS/dLogD_{em}$; $\mu m^2\ cm^{-3}$) and volume ($dV/dLogD_{em}$; $\mu m^3\ cm^{-3}$) PSDs assuming spherical particles, and further transformed into mass PSDs ($dM/dLogD_{em}$; $\mu g\ m^{-3}$) using the bulk density of KCl, $\rho_p = 1.98\ g\ cm^{-3}$, as reported by Wu and Boor (2020). Median PSDs were utilized to compute size-integrated concentrations for number (N), surface area (S), volume (V), and mass (M). The concentration flux through the test rig was then calculated as the product of the respective size-integrated concentration and the volumetric airflow rate.

Lognormal distribution functions are widely used to model PSDs due to their ability to capture realistic aerosol characteristics. Compared to unimodal fits, bimodal lognormal functions more accurately represent TAG-generated KCl aerosol by capturing distinct peaks or overlapping modes observed experimentally. Therefore, the median number PSDs measured by the SMPS were fitted using a bimodal lognormal distribution function:

$$\frac{dN}{dLogD_{em}} = \sum_{i=1}^{2} \frac{N_i}{(2\pi)^{\frac{1}{2}} \log(\sigma_i)} \exp\left[-\frac{\left(\log D_{em} - \log \overline{D_{em,i}}\right)^2}{2\log^2(\sigma_i)}\right] \quad (1)$$

where $\overline{D_{em,i}}$ is the geometric mean diameter (modal diameter) for mode i, σ_i is the geometric standard deviation for mode i, and N_i is the number concentration (modal amplitude) for mode i. These parameters were determined using least squares fitting in MATLAB (The MathWorks, Inc., Natick, MA, USA). The same fitting approach was applied to the other PSD categories, with N_i replaced with the surface area (S_i), volume (V_i), or mass (M_i) concentration for mode i. A bimodal lognormal distribution (two modes) was

Table 2. Description of instrumentation used in the HVAC filter test rig.

Instrument	Manufacturer	Model	Accuracy	Range	Function
Pressure transducers	Setra Systems, Inc.	Model 276	±0.25%	600 to 1100 mb	Barometric pressure measurement
		Model 265	±0.25%	0 to 5 in H_2O	Differential pressure transducer for filter ΔP measurement
			±0.25%	0 to 0.5 in H_2O	Differential pressure transducer for volumetric airflow rate measurement
Temperature & RH transmitter	Setra Systems, Inc.	Model SRH200	±2.5% RH ±0.3 °C	0 to 100% RH −40 to 60 °C	Sensor for monitoring in-duct temperature and RH
Pitot-tubes	Dwyer Instruments LLC	Model 160	±2 − 5%	400 to 20,000 ft min^{-1}	Air velocity measurement
Data acquisition board	National Instruments, Inc.	Model 6211	±2.69 mV	AO/I: ±10 V	Data acquisition for voltage signals and control
HR-ELPI+	Dekati Ltd.	–	–	6 to 10,000 nm	Aerosol number-based PSD measurement
SMPS	TSI, Inc.	Model 3938NL88	–	20.1 to 1000 nm with long DMA	Aerosol number-based PSD measurement
Combustion gas detector	General Tools, Inc.	Model NGD269	±50 ppm	0 to 20,000 ppm	Monitoring of C_3H_8 leakage

found to best fit the PSDs in all cases. Time-series plots of number and mass PSDs demonstrated TAG operational stability and repeatability of KCl aerosol output. Normalized PSDs for number, surface area, volume, and mass were grouped to assess the effects of experimental conditions on salt aerosol properties. PSDs of TAG-generated KCl aerosol were compared with urban aerosol size distributions to validate their suitability for aging HVAC filters and evaluating filter performance.

Calculation of particle deposition in the aerosol sampling manifold

The aerosol sampling manifold transports particles from the HVAC filter test rig to the SMPS and HR-ELPI+ for PSD measurement. During transport, particles can be lost due to several deposition mechanisms. Inlet efficiency (η_{inlet}) accounts for particle losses at the sample probe inlet caused by mismatched air velocities between the sample line and in-duct airflow. Gravitational settling efficiency ($\eta_{tube,grav}$) describes particle deposition on sample line walls under the influence of gravity. Diffusional deposition efficiency ($\eta_{tube,diff}$) results from Brownian motion, where particles diffuse from higher-concentration sample airflow streams to lower concentration regions along the sample line walls. Inertial deposition efficiency ($\eta_{inert,bend}$) occurs when particles deviate from the airflow stream and deposit on walls during redirection through bends in the sample line. The total aerosol transport efficiency is calculated as the product of these individual transport efficiency terms ($\eta_{total} = \eta_{inlet} \times \eta_{tube,grav} \times \eta_{tube,diff} \times \eta_{inert,bend}$), with each term calculated following the modeling methods described in Chapter 6 of Kulkarni et al. (2011). By accounting for both aerosol transport efficiency and the DF of the dilution system, we can calculate the actual in-duct number PSDs as follows:

$$\left(\frac{dN}{dLogD_{em}}\right)_{in-duct} = \left(\frac{dN}{dLogD_{em}}\right)_{measured} \div \eta_{total} \times DF \quad (2)$$

Results and discussion

This section presents the operational characteristics of the test rig and TAG. First, the raw PSDs of the KCl aging aerosol measured under varying experimental conditions are outlined, along with the corresponding lognormal fitting parameters. The PSDs of TAG-generated KCl aerosol are compared with urban atmospheric aerosol number and mass PSDs, as well as with existing loading dusts commonly used in HVAC filtration studies. Key operational parameters of the test rig, including in-duct volumetric airflow rates, RH levels, and velocity and aerosol concentration uniformity, are also analyzed. Lastly, the calculation of dilution factors and aerosol deposition losses within the sampling manifold is presented. The results confirm the reliable operation of the TAG integrated with the test rig, demonstrating its suitability and repeatability for rapidly aging HVAC filters and assessing long-term energy consumption as per the proposed ASHRAE Guideline 35. The PSD results, including lognormal fitting parameters, serve as a valuable reference for future applications of ASHRAE Guideline 35.

Uniformity of in-duct cross-sectional air velocities and TAG-generated KCl aerosol concentrations in the HVAC filter test rig

Uniformity assessments of air velocity and TAG-generated submicrometer KCl aerosol concentrations were conducted upstream of the test-filter section using a nine-point traverse evenly distributed across the duct cross section, in accordance with ANSI/ASHRAE Standard 52.2 (ASHRAE 2017). Figure 3 presents the size-integrated number concentrations of TAG-generated KCl aerosol and the corresponding air velocities at each traverse point. Elevated particle concentrations and air velocities were observed at points 1, 4, and 7, indicating locally higher aerosol loading across that region of the test filter. Air velocity measurements demonstrated good uniformity, with a coefficient of variation (COV) of

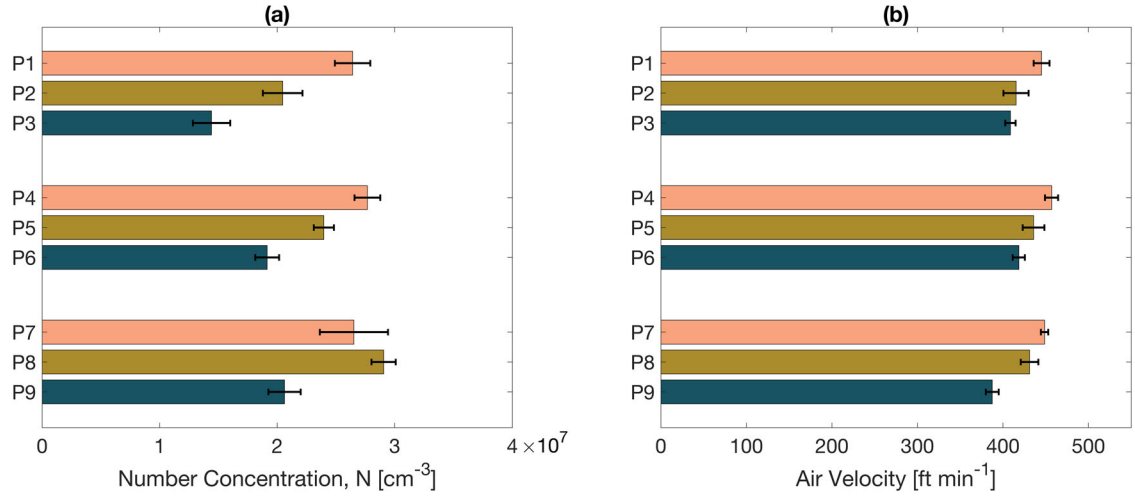

Fig. 3. Uniformity of in-duct cross-sectional KCl aerosol number concentrations (size-integrated across D_a = 6 to 10,000 nm; measured by the HR-ELPI+) and air velocities, evaluated using a nine-point traverse. Points 1 to 3 (P1 to P3), 4 to 6 (P4 to P6), and 7 to 9 (P7 to P9) lie on common horizontal planes, with each group evenly spaced along the vertical axis of the cross-sectional area. The figure illustrates relative variations across measurement points to assess spatial uniformity.

5.2%, satisfying the ANSI/ASHRAE Standard 52.2 requirement of COV < 10%. While the standard does not mandate uniformity for loading dusts, the spatial distribution of TAG-generated KCl aerosol number concentrations was also evaluated. The resulting COV was 20.7%, slightly above the standard's COV < 15% criterion for test aerosol used in filtration efficiency testing. However, since the goal of this methodology is to simulate filter loading rather than assess efficiency, the observed aerosol distribution was deemed acceptable for the study's objectives.

Measured particle size distributions of the TAG-generated KCl aerosol

An illustrative number PSD time-series measured with the HR-ELPI+ during a MERV 14 baseline loading experiment is shown in Figure 4, demonstrating the stability of KCl aerosol output from the TAG. The number PSD shape remains consistent throughout the experiment, with peak concentrations occurring around $D_a \approx 100$ nm. Most of the number concentration is within the range of $D_a = 30$ to 300 nm, indicating that the TAG-generated KCl aerosol predominantly resides in the Aitken and accumulation modes. Consistency in the peak concentration magnitude is evident from the uniform color bar scale of the highest concentration and the similar height of the size-integrated total number concentrations, which range from 1.5 to 2×10^7 cm^{-3}. Minor fluctuations are attributed to variations in TAG operation or airflow conditions within the test rig. Overall, the TAG-generated submicrometer KCl aerosol output was stable and consistent during the loading experiments. The difference in number concentration magnitude between the upstream and downstream locations of the test filter underscores the high filtration efficiency of the MERV 14 filter. This filtration effect is further illustrated in Figure 5, which compares the median PSDs measured upstream and downstream of the test filter over the entire baseline experimental period, using the same axis scale. A clear reduction in particle concentrations across the size spectrum is evident, demonstrating the effectiveness of the MERV 14 filter in removing the KCl aerosol.

Figure 5 illustrates the number, surface area, volume, and mass PSDs for both upstream and downstream measurements as a function of D_{em} (via SMPS measurements). Upstream data consistently show high concentrations across all metrics, reflecting sufficient submicrometer aerosol generation around $D_{em} \approx 100$ nm. The PSDs represent the median values over the entire aging period for all baseline MERV 14 experiments. Substantial concentration differences between upstream and downstream PSDs highlight the high filtration efficiency of the MERV 14 test filters. This gap serves as an indicator of filter media integrity, as any damage or airflow bypass would reduce the concentration difference. Although this methodology is not specifically designed to evaluate filtration efficiency, upstream and downstream comparisons offer valuable insights into the evolution of efficiency during HVAC filter aging. These findings enhance understanding of filter aging dynamics and their associated energy implications, as dust loading affects both filtration

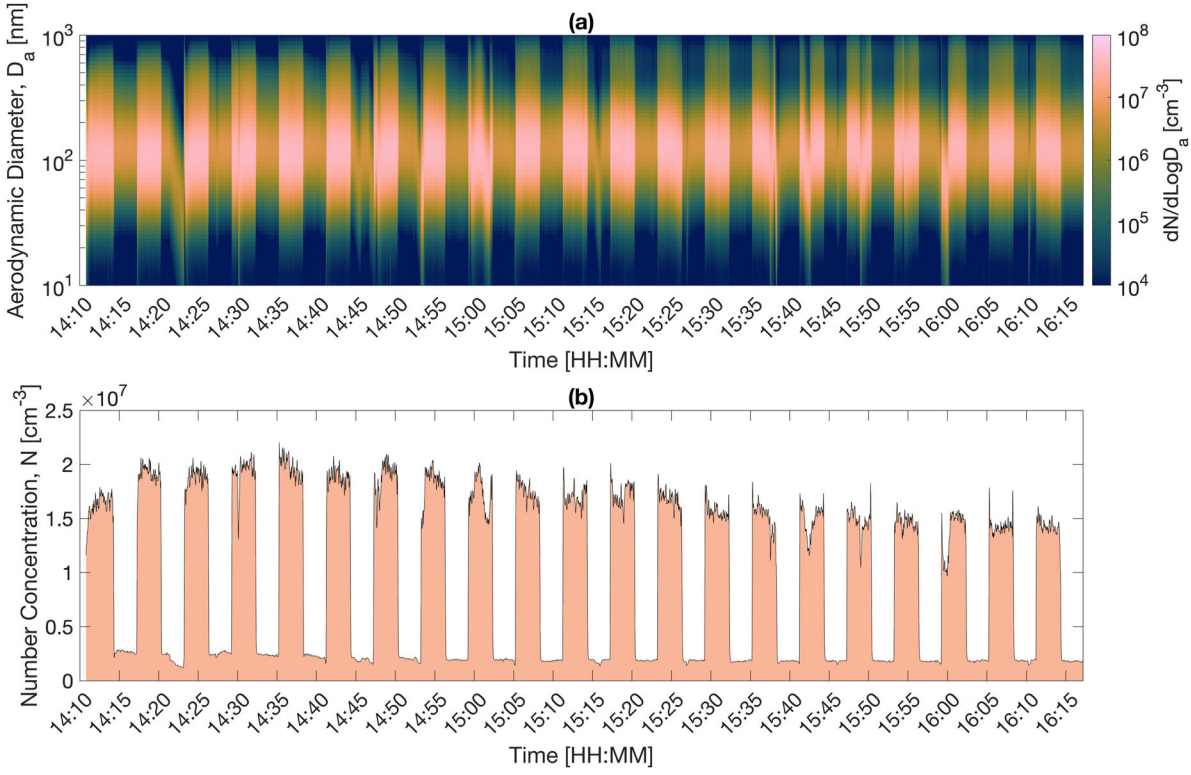

Fig. 4. Time-series plots of TAG-generated submicrometer KCl aerosol: (a) number PSDs and (b) size-integrated number concentrations ($D_a = 6$ to 10,000 nm) measured by the HR-ELPI+ during baseline aging conditions. Sampling alternated every 3 min between upstream and downstream of a MERV 14 test filter.

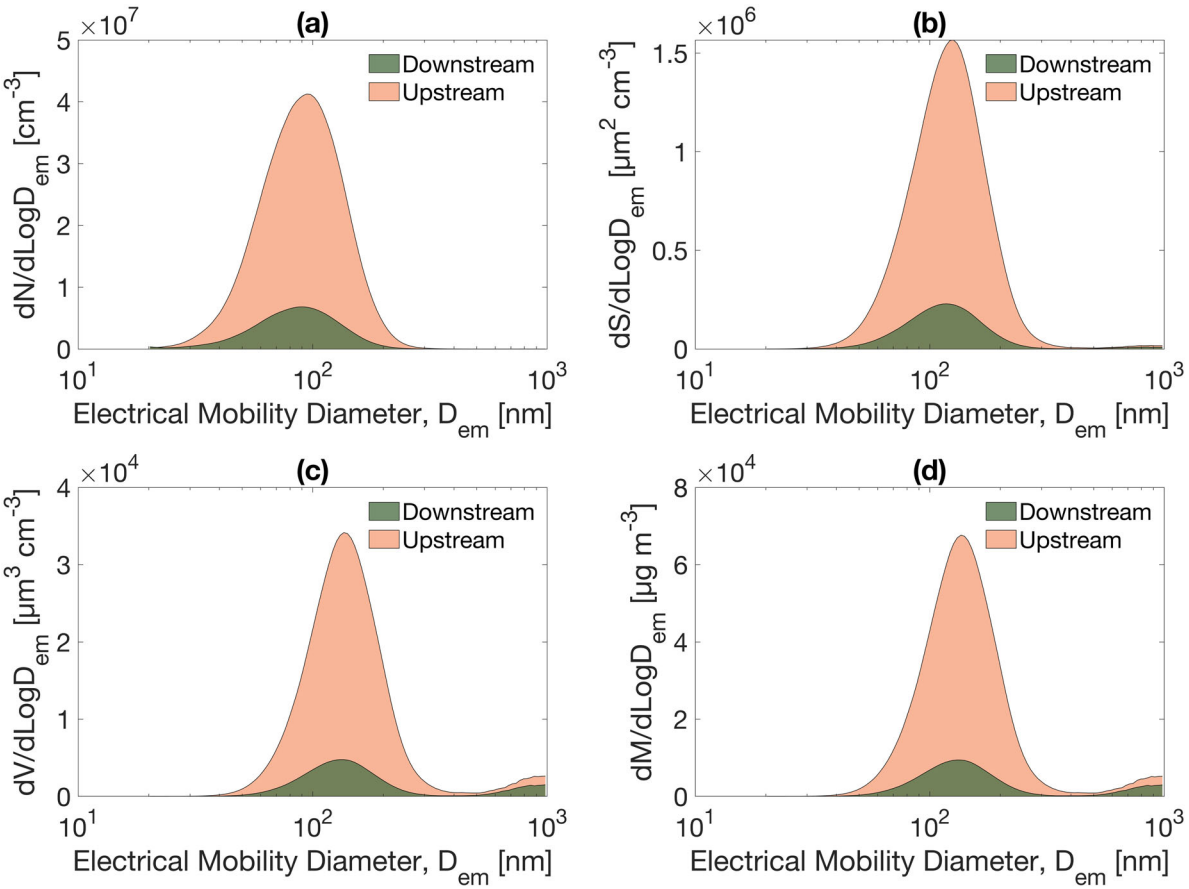

Fig. 5. Comparison of upstream and downstream median PSDs: (a) number, (b) surface area, (c) volume, and (d) mass PSDs for all MERV 14 test filters under baseline aging conditions (via SMPS measurements).

efficiency and filter pressure drop (ΔP), thereby impacting blower energy consumption during operation. Together, Figures 4 and 5 provide a reference for monitoring TAG-generated KCl aerosol output of the TAG under baseline loading conditions and for comparisons with sensitivity test conditions.

Figure 6 presents PSDs measured by the SMPS across different metrics: number (a, b), surface area (c, d), and volume and mass (e, f), summarized from all baseline aging experiments for all test filter types. The black curve denotes the median PSD, while the shaded region represents the interquartile range (IQR; 25th–75th percentile). Lognormal fitting was applied to the median PSDs. Median number PSDs for TAG-generated KCl aerosol exhibit a unimodal distribution with a prominent submicrometer peak ($D_{em} \approx$ 100 nm). The peaks are relatively narrow, with geometric standard deviations between 1.2 and 1.5, indicating a uniform distribution around the modal diameter. The median PSDs shift toward larger sizes when transitioning from number to surface area PSDs, and further to volume and mass PSDs. A secondary peak near $D_{em} \approx$ 1000 nm appears in the volume and mass PSDs, likely attributed to MgO binding agents from salt stick ash blown off by the high-velocity blowtorch flow, rather than KCl aerosol formed via evaporation-condensation in the high-temperature O_2–C_3H_8 flame. In addition, prior work by Wu and Boor (2020) reported a partial secondary sub-20 nm peak of nanosized soot particles generated by the TAG, attributed to soot precursors or organic carbon formed in the O_2–C_3H_8 flame (Wu and Boor 2020), consistent with high-temperature propane combustion chemistry that produces polycyclic aromatic hydrocarbons (PAHs) and soot nuclei via dehydrogenation, polymerization, cyclization, and radical chain reactions (Johansson et al. 2018; Frenklach and Mebel 2020).

A bimodal lognormal distribution function was applied to PSDs from all sensitivity tests, covering aging conditions of 1000 ft^3 min^{-1}, 500 ft^3 min^{-1}, 18 mm min^{-1}, 5 mm min^{-1}, 57.5 ± 2.5% RH, and 27.5 ± 2.5% RH, as summarized in Supplementary Figures S1 to S6 and Table 3. These parameters offer critical inputs for modeling efforts aimed at replicating TAG-generated PSDs and simulating filter aging behavior. Overall, the PSDs exhibit consistent unimodal distributions across all aging conditions, with a prominent submicrometer peak. While minor variations in peak concentration are observed, the values remain within the same order of magnitude regardless of the aging condition. No discernible trends in peak concentration emerge across different sensitivity tests; however, within the same test category, modal diameter shifts in response to changing conditions. For example, reduced volumetric airflow rates correspond to larger particle diameters. For direct comparison,

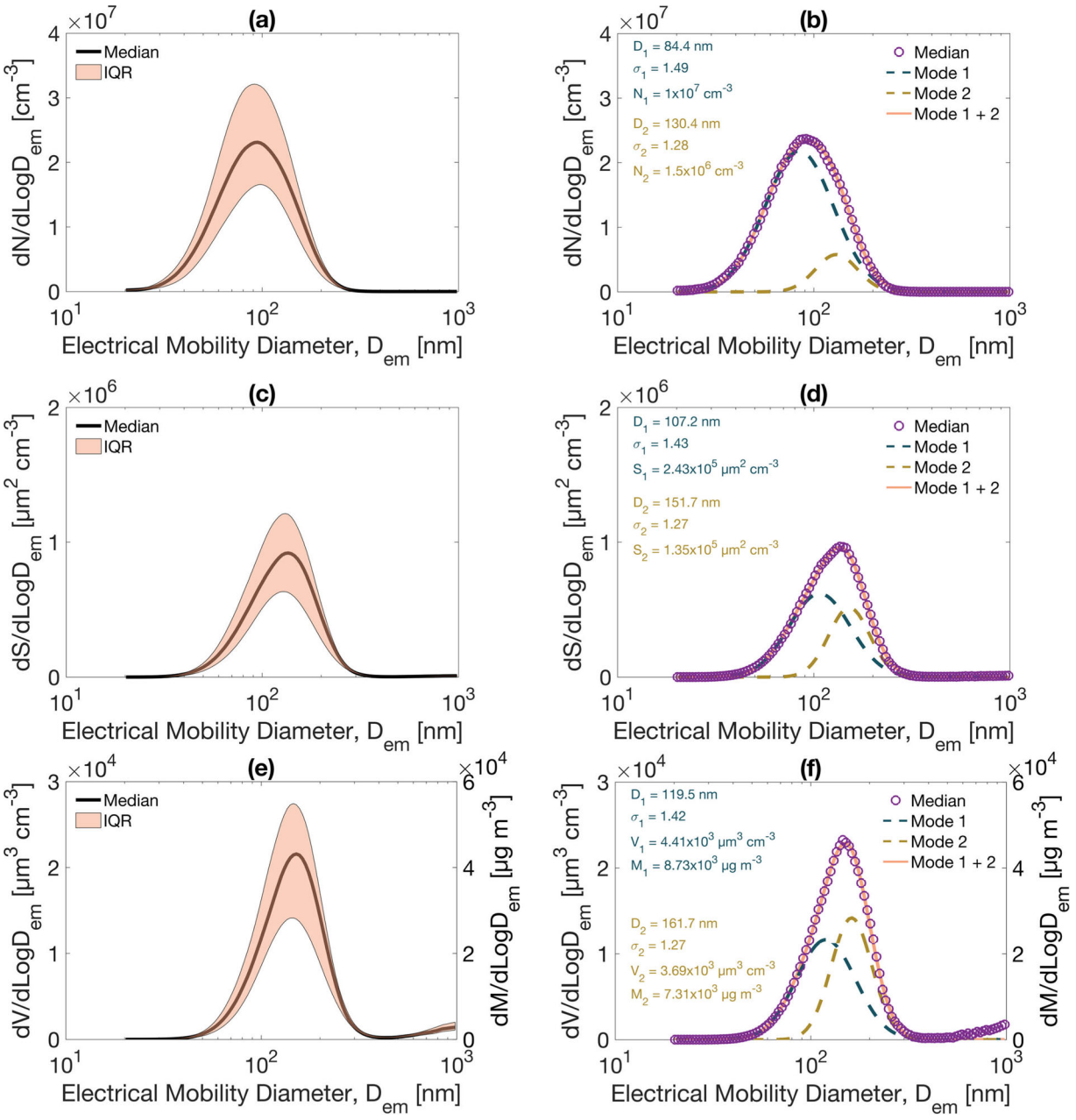

Fig. 6. (a, b) Number, (c, d) surface area, and (e, f) volume and mass PSDs for upstream TAG-generated submicrometer KCl aerosol, summarized across all baseline aging experiments for all test filter types. The black curve represents the median PSD, while the shaded region indicates the IQR (25th–75th percentile). Bimodal lognormal fit parameters are shown in the upper left of (b, d, f).

normalized PSDs are plotted together and grouped by sensitivity test category, highlighting shifts in modal diameters under varying conditions.

The normalized median PSDs for sensitivity tests on the volumetric airflow rate, salt stick feed rate, and RH levels are compared in Figures 7 to 9, respectively. Normalized PSDs were obtained by dividing the concentration of each size bin by the maximum observed concentration. In the volumetric airflow rate sensitivity tests (Figure 7), the peak positions of number PSDs shift toward larger particle sizes as the volumetric airflow rate decreases from 2000 to 500 ft^3 min^{-1}. Specifically, the peak particle diameter increases from $D_{em} \approx 90$ nm at 2000 ft^3 min^{-1} to $D_{em} \approx 110$ nm at 500 ft^3 min^{-1}. Similar trends have been reported in other studies (Ma et al. 2022; Morawska et al. 2022; Hu et al. 2024), where reduced volumetric airflow rates increase particle residence time, enhancing opportunities for coagulation and shifting the PSD toward larger sizes. Correspondingly, the mass PSDs also show a shift toward larger peak diameters, though the magnitude is smaller. This occurs because mass distributions are dominated by larger particles, whereas number distributions are more sensitive to changes across all particle sizes, leading to more noticeable shifts in peak positions.

Table 3. Bimodal lognormal fitting parameters for KCl PSDs across all aging conditions.

PSD type	Experiment type	Volumetric airflow rate [$ft^3\ min^{-1}$]	RH [± 2.5%]	Salt stick feed rate [mm min^{-1}]	Mode 1			Mode 2		
					Modal amplitude N_1, S_1, V_1, M_1	Modal diameter $\bar{D}_{em,1}$ [nm]	Geometric standard deviation σ_1 [-]	Modal amplitude N_2, S_2, V_2, M_2	Modal diameter $\bar{D}_{em,2}$ [nm]	Geometric standard deviation σ_2 [-]
Number [cm^{-3}]	Baseline experiments	2000	42.5	10	1.0×10^7	84.4	1.49	1.5×10^6	130.4	1.28
	Volumetric airflow rate	1000	42.5	10	1.2×10^7	92	1.44	5.1×10^6	137.3	1.29
	sensitivity experiments	500	42.5	10	3.5×10^6	75.7	1.37	9.0×10^6	122.1	1.36
	Salt stick feed rate	2000	42.5	18	5.6×10^6	80	1.39	5.4×10^6	125.3	1.35
	sensitivity experiments	2000	42.5	5	8.8×10^6	68.6	1.49	2.6×10^6	98	1.29
	RH sensitivity	2000	57.5	10	6.8×10^6	74	1.47	4.4×10^6	105.3	1.34
	experiments	2000	27.5	10	1.2×10^7	88.3	1.5	2.9×10^6	155.3	1.3
Surface area	Baseline experiments	2000	42.5	10	2.43×10^5	107.2	1.43	1.35×10^5	151.7	1.27
[$\mu m^2\ cm^{-3}$]	Volumetric airflow rate	1000	42.5	10	3.53×10^5	113.7	1.41	3.98×10^5	157	1.3
	sensitivity experiments	500	42.5	10	3.51×10^5	128	1.44	2.28×10^5	156.6	1.3
	Salt stick feed rate	2000	42.5	18	8.35×10^4	86.1	1.3	3.72×10^5	145.2	1.35
	sensitivity experiments	2000	42.5	5	1.53×10^5	89.4	1.47	1.12×10^5	112.8	1.3
	RH sensitivity	2000	57.5	10	1.44×10^5	93.7	1.42	1.92×10^5	128.3	1.33
	experiments	2000	27.5	10	2.15×10^5	98.5	1.4	4.63×10^5	168.9	1.36
Volume	Baseline experiments	2000	42.5	10	4.41×10^3	119.5	1.42	3.69×10^3	161.7	1.27
[$\mu m^3\ cm^{-3}$]	Volumetric airflow rate	1000	42.5	10	6.95×10^3	126.8	1.4	1.09×10^4	168.3	1.29
	sensitivity experiments	500	42.5	10	1.36×10^4	156	1.39	5.18×10^2	177.3	1.11
	Salt stick feed rate	2000	42.5	18	7.92×10^2	85.1	1.24	9.87×10^3	156.3	1.36
	sensitivity experiments	2000	42.5	5	2.19×10^3	101.7	1.47	2.44×10^3	120.6	1.31
	RH sensitivity	2000	57.5	10	3.04×10^3	108.5	1.4	3.59×10^3	142.9	1.31
	experiments	2000	27.5	10	4.77×10^3	118.8	1.43	1.26×10^4	188	1.35
Mass	Baseline experiments	2000	42.5	10	8.73×10^3	119.5	1.42	7.31×10^3	161.7	1.27
[$\mu g\ m^{-3}$]	Volumetric airflow rate	1000	42.5	10	1.38×10^4	126.8	1.4	2.16×10^4	168.3	1.29
	sensitivity experiments	500	42.5	10	2.7×10^4	156	1.39	1.03×10^3	177.3	1.11
	Salt stick feed rate	2000	42.5	18	1.57×10^3	85.1	1.24	1.96×10^4	156.3	1.36
	sensitivity experiments	2000	42.5	5	4.33×10^3	101.7	1.47	4.83×10^3	120.6	1.31
	RH sensitivity	2000	57.5	10	6.03×10^3	108.5	1.4	7.1×10^3	142.9	1.31
	experiments	2000	27.5	10	9.45×10^3	118.8	1.43	2.5×10^4	188	1.35

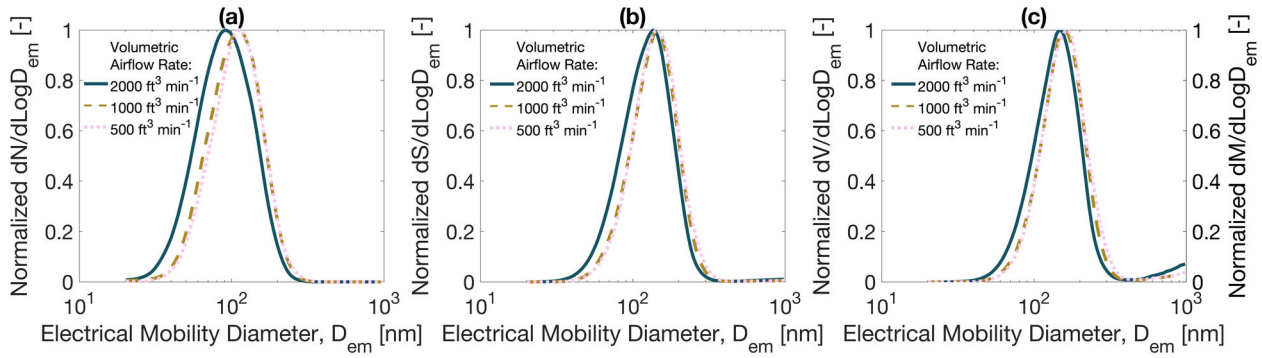

Fig. 7. Normalized median (a) number, (b) surface area, and (c) volume and mass PSDs for TAG-generated upstream submicrometer KCl aerosol at a salt stick feed rate of 10 mm min^{-1}; RH of 42.5 ± 2.5%; and volumetric airflow rates of 2000 ft^3 min^{-1} (blue line), 1000 ft^3 min^{-1} (yellow dashed line), and 500 ft^3 min^{-1} (pink dotted line).

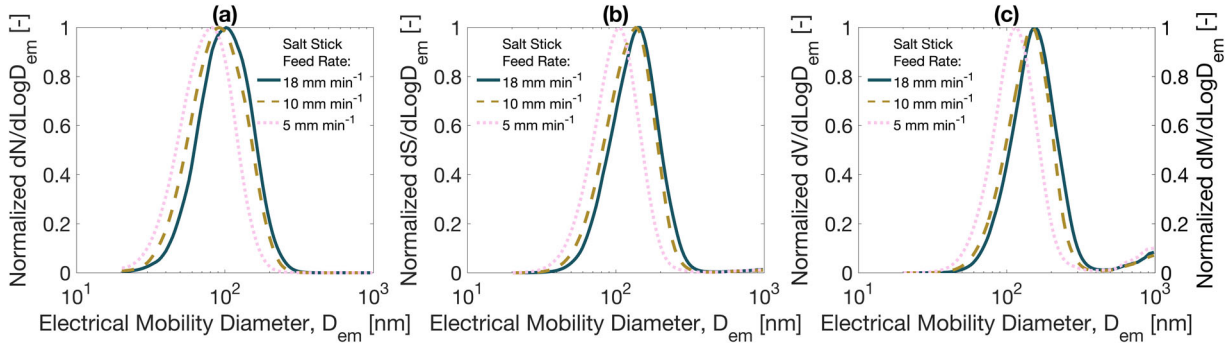

Fig. 8. Normalized median (a) number, (b) surface area, and (c) volume and mass PSDs for upstream TAG-generated submicrometer KCl aerosol at salt stick feed rates of 18 mm min^{-1} (blue line), 10 mm min^{-1} (yellow dashed line), and 5 mm min^{-1} (pink dotted line); RH of 42.5 ± 2.5%; and volumetric airflow rate of 2000 ft^3 min^{-1}.

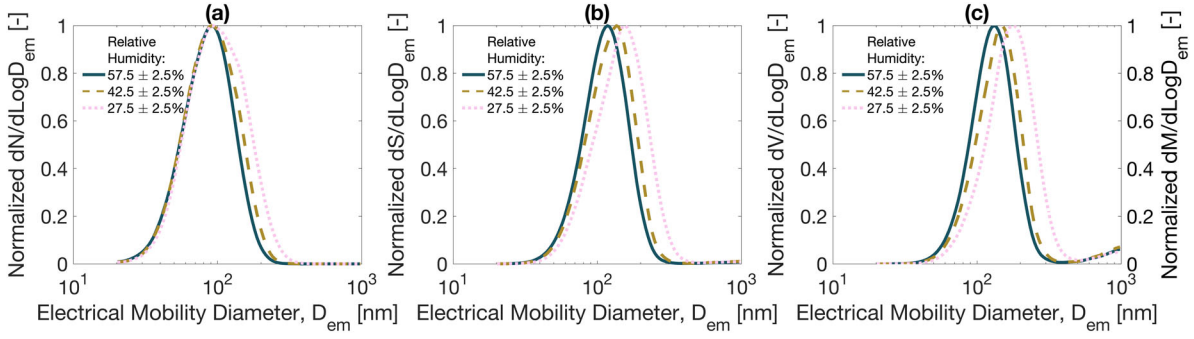

Fig. 9. Normalized median (a) number, (b) surface area, and (c) volume and mass PSDs for upstream TAG-generated submicrometer KCl aerosol at a salt stick feed rate of 10 mm min^{-1}; RH of 57.5 ± 2.5% (blue line), 42.5 ± 2.5% (yellow dashed line), and 27.5 ± 2.5% (pink dotted line); and volumetric airflow rate of 2000 ft^3 min^{-1}.

The salt stick feed rate sensitivity tests (Figure 8) show a clear upward trend in peak diameters as the feed rate increases. The peak number diameter rises from $D_{em} \approx$ 78 nm at a feed rate of 5 mm min^{-1} to $D_{em} \approx$ 101 nm at 18 mm min^{-1}. Similarly, the mass PSDs also shift toward larger diameters, reflecting the trend observed in the number PSDs. This behavior aligns with findings from other aerosol generation techniques (Chen et al. 2019; Neo et al. 2022), where higher feed rates increase particle diameters. Higher feed rates promote particle coalescence and agglomeration due to increased particle–particle interactions. With more particles generated in a shorter time, collisions and agglomeration become more likely, increasing particle size. Conversely, slower feed rates result in a higher proportion of small soot particles ($D_{em} < 20$ nm) produced by the O_2–C_3H_8 flame, shifting the PSD toward smaller particles, as seen at the 5 mm min^{-1} feed rate.

Notably, the peak locations of the number PSDs remain consistent across different RH levels (Figure 9). However, a secondary mode around $D_{em} \approx$ 150 nm becomes more

pronounced at 47.5 ± 2.5% and 27.5 ± 2.5% RH compared to 57.5 ± 2.5% RH. This secondary mode shifts the peak of the mass PSDs toward larger particle diameters at 47.5 ± 2.5% and 27.5 ± 2.5% RH, with a more pronounced shift at 27.5 ± 2.5%. This finding contrasts with studies (McMurry and Stolzenburg 1989; Gupta et al. 1993; Weingartner et al. 1995; Reponen et al. 1996; Hu et al. 2010; Cummings et al. 2020) showing that higher RH typically increases particle size for hygroscopic aerosol. In this case, the PSD shifts for TAG-generated KCl aerosol may be more influenced by electrostatic charges, likely elevated due to the high-temperature O_2–C_3H_8 flame. Previous studies (Fialkov et al. 1997; Sgro et al. 2010; Wang et al. 2017) report that high-temperature flames generate substantial concentrations of charged ions ($\sim 10^{10}$ cm^{-3}) that attach to particles, promoting agglomeration and larger particle sizes. However, RH moderates this process: higher water vapor levels at 57.5 ± 2.5% RH effectively reduce electrostatic charges on particles, inhibiting agglomeration and resulting in smaller peak diameters.

The shape of the number PSDs for all sensitivity tests closely resembles those reported in urban environments across various global regions (Figure 10) (Wu and Boor 2021). Notably, the number PSDs of TAG-generated KCl aerosol at an airflow rate of 500 ft^3 min^{-1} align well with urban aerosol number PSDs measured in Central, South, and Southeast Asia (CSSA), particularly the prominent peak ($D_{em} \approx 105$ nm). Additionally, the secondary peak of the CSSA number PSDs ($D_{em} \approx 70$ nm) is represented by TAG-generated KCl aerosol at a salt stick feed rate of 5 mm min^{-1}, where the peak diameter is $D_{em} \approx 80$ nm. While single TAG-generated KCl aerosol settings cannot fully replicate multimodal urban aerosol number PSDs, future work could explore using two TAGs to simulate bimodal PSDs, more accurately reflecting urban conditions like those in CSSA. The TAG-generated KCl aerosol also effectively simulates number PSDs observed in East Asia (EA). Specifically, the PSDs of TAG-generated KCl aerosol at a 5 mm min^{-1} feed rate closely align with the EA region's prominent peak ($D_{em} \approx 70$ nm), corresponding to a KCl peak diameter of $D_{em} \approx 80$ nm. Overall, the number PSDs of the TAG aerosol produced by the TAG have peak diameters consistent with those observed in urban environments globally; however, they are shifted toward larger sizes compared to those reported in North America, Australia, and New Zealand (NAAN), Europe (EU), and Latin America (LA).

There is limited literature addressing the generation of submicrometer loading aerosol for full-scale HVAC filter testing. The normalized number PSDs of alumina ($Al(OH)_3$) dust particles from Giffin et al. (Giffin et al. 2012) are shown in Figure 10, highlighting a larger peak particle diameter ($D_{em} \approx$ 200 nm) compared to most urban aerosol PSDs and the TAG-generated KCl aerosol. This difference suggests distinct loading kinetics when $Al(OH)_3$ dust is used, as its larger particles are likely to promote the formation of more porous dust cakes, leading to a slower increase in the test filter ΔP and an overestimation of dust holding capacity (Poon and Liu 1997a; Lee et al. 2001; Giffin et al. 2012; Wang et al. 2016).

Figure 11 compares the normalized volume PSDs of TAG-generated KCl aerosol with the global median urban aerosol mass PSD reported by Wu and Boor (2021), as well as the volume PSDs of standardized loading test dusts commonly used in full-scale HVAC filter testing, including ISO 12103-1: A0 to A4 test dusts (Hanley et al. 1994, 1999; Raynor and Soo 2003; Knobloch et al. 2024). While the coarse-mode peak (between 1000 and 10,000 nm) of the

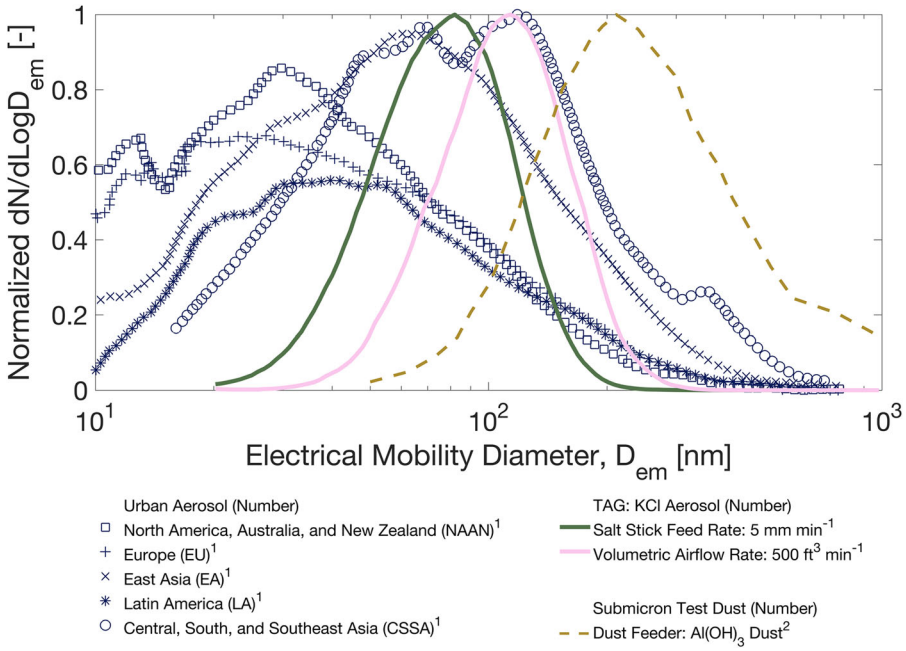

Fig. 10. Normalized median number PSDs of TAG-generated KCl aerosol under different experimental settings. These are compared with median urban aerosol number PSDs from various geographical regions as reported in (1)Wu and Boor (2021) and the number PSD of $Al(OH)_3$ dust generated and measured in a full-scale HVAC filter loading test stand as reported in (2) Giffin et al. (2012).

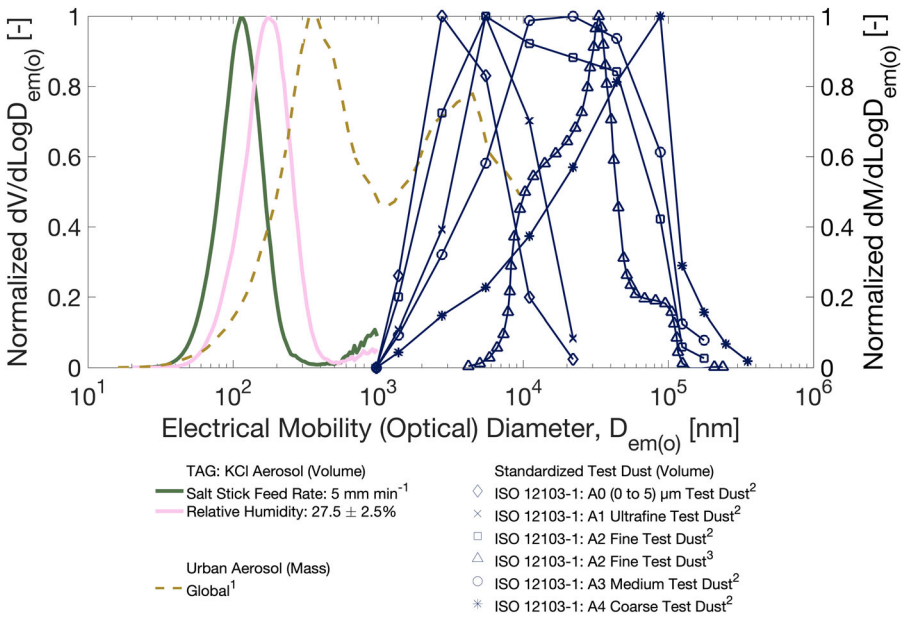

Fig. 11. Normalized median volume PSDs of TAG-generated KCl aerosol under different experimental settings. These are compared with the global median urban aerosol mass PSD as reported in (1) Wu and Boor (2021); volume PSDs of ISO 12103-1: A0 to A4 test dusts as specified in ISO (2024) and measured using a light-scattering particle size analyzer; and the volume PSD of ISO 12103-1: A2 test dust generated and measured in situ using a laser-based shadowgraph optical technique as reported in (3) Kang et al. (2018). The volume PSDs of ISO 12103-1: A0 to A4 test dusts are based on optical diameters (D_o), consistent with the use of optical-based measurement techniques.

global median urban aerosol mass PSD is less prominent than the accumulation mode peak (between 100 and 1000 nm), it closely aligns with coarse standardized test dusts such as ISO 12103-1: A0 and A1. In contrast, the TAG-generated KCl aerosol more accurately replicates the accumulation mode peak of the urban aerosol mass PSD, albeit with a slightly smaller median diameter than in typical urban profiles. Notably, standardized loading dust PSDs often deviate from their specification targets (Figure 11). For example, Kang et al. (Kang et al. 2018) reported that ISO 12103-1: A2 test dust generated using an ISO injector exhibited a broader PSD and shifted toward larger particle diameters due to resuspension and limited deagglomeration. Their in situ measurements showed a peak diameter of ~35,000 nm, significantly larger than the standard-specified value. These discrepancies suggest that standardized test dusts may poorly represent the real-world aerosol exposures encountered by HVAC filters.

Collectively, the submicrometer KCl aerosol generated by the TAG more closely matches the submicrometer fraction of urban aerosol number and mass PSDs reported by Wu and Boor (2021) than do the standardized ISO 12103-1: A0 to A4 test dusts. While TAG-generated aerosol effectively replicates the accumulation mode of the global median urban mass PSD, it lacks the coarse-mode particles needed to capture the secondary peak observed between 1000 and 10,000 nm (Figure 11). Additionally, the TAG-generated KCl aerosol PSDs do not consistently align with the exact peak diameters or shapes of urban number and mass PSDs. Urban aerosol number PSDs typically exhibit broader, multimodal distributions skewed toward smaller particles (e.g.,

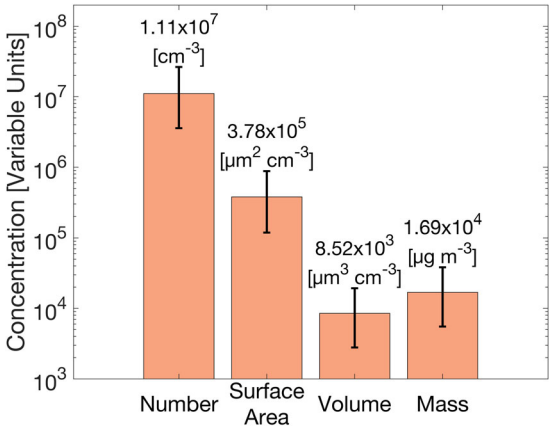

Fig. 12. Size-integrated number, surface area, volume, and mass concentrations upstream of the test filter summarized across all baseline experiments. Bar heights represent median values, and error bars indicate the IQR (25th–75th percentile). Calculations are integrated across a size range of D_{em} = 20 to 982 nm, using a bulk density of ρ_p = 1.98 g cm^{-3} for mass concentration estimates.

NAAN and EU regions), in contrast to the unimodal PSDs produced by TAG-generated KCl aerosol. These smaller particles can accelerate increases in filter ΔP during loading and reduce dust holding capacity, suggesting that TAG-generated aerosol may underestimate ΔP growth and overestimate dust holding capacity. Unlike urban environments, where multiple aerosol sources and transformation processes yield distinct modes, including a third mode of ~350 nm in the CSSA region, the TAG output at a fixed setting produces

only unimodal distributions. Larger particles in the ~350 nm mode promote surface filtration, thereby slowing filter ΔP growth. Furthermore, previous studies (Endo et al. 1998a; Viswanathan et al. 2015) have shown that the most penetrating particle size (MPPS) for filters shifts from ~200 nm to ~100 nm during loading, further complicating performance evaluations in regions with prominent larger aerosol modes, such as CSSA. Despite these limitations, TAG-generated aerosol remains a substantially better proxy for urban aerosol conditions than standardized coarse-mode loading dusts.

Size-integrated concentrations and fluxes of TAG-generated KCl aerosol in the HVAC filter test rig

Figure 12 presents the size-integrated (D_{em} = 20 to 982 nm) number, surface area, volume, and mass concentrations of TAG-generated KCl aerosol. Bar heights represent median values, while error bars indicate the IQR (25th–75th percentile). Data were compiled from 15 baseline experiments across various test filter types. The median size-integrated number concentration is approximately $1.11 \times 10^7\,cm^{-3}$, which is three to four orders of magnitude higher than typical urban aerosol number concentrations (10^3 to $10^4\,cm^{-3}$) (Wu and Boor 2021). Similarly, the size-integrated mass concentration is elevated by two to three orders of magnitude compared to outdoor aerosol levels, typically 10^1 to $10^2\,\mu g\ m^{-3}$ (Tofful et al. 2021; Wu et al. 2024). This mass concentration is comparable to levels achieved by loading dusts composed of coarse-mode particles in other studies, which are on the order of $10^4\,\mu g\ m^{-3}$ (Lee et al. 2020; Li et al. 2022). Collectively, the TAG-generated KCl aerosol successfully achieved the elevated number and mass concentrations necessary for the accelerated aging of HVAC filters, as required by the forthcoming ASHRAE Guideline 35.

The size-integrated concentration fluxes for three volumetric airflow rate settings of the test rig are shown in Figure 13. Bar heights represent median values, with error bars indicating the IQR (25th–75th percentile). These fluxes reflect the estimated TAG-generated KCl aerosol production per minute, as determined via SMPS measurements (D_{em} = 20 to 982 nm) taken upstream of the test filter. The aerosol mass flux achieved in the test rig is orders of magnitude higher than those typically observed in commercial HVAC systems (Wu et al. 2024), and is comparable to the mass flux of coarse-mode loading dusts (~$10^6\,\mu g\ min^{-1}$) used in other filtration studies (Hanley et al. 1994). Fluxes remain stable between volumetric airflow rates of 2000 and 1000 $ft^3\ min^{-1}$ but decrease at 500 $ft^3\ min^{-1}$, likely due in part to incomplete aerosol intake through the 90° aerosol injection elbow, which may allow some KCl aerosol to escape the test rig.

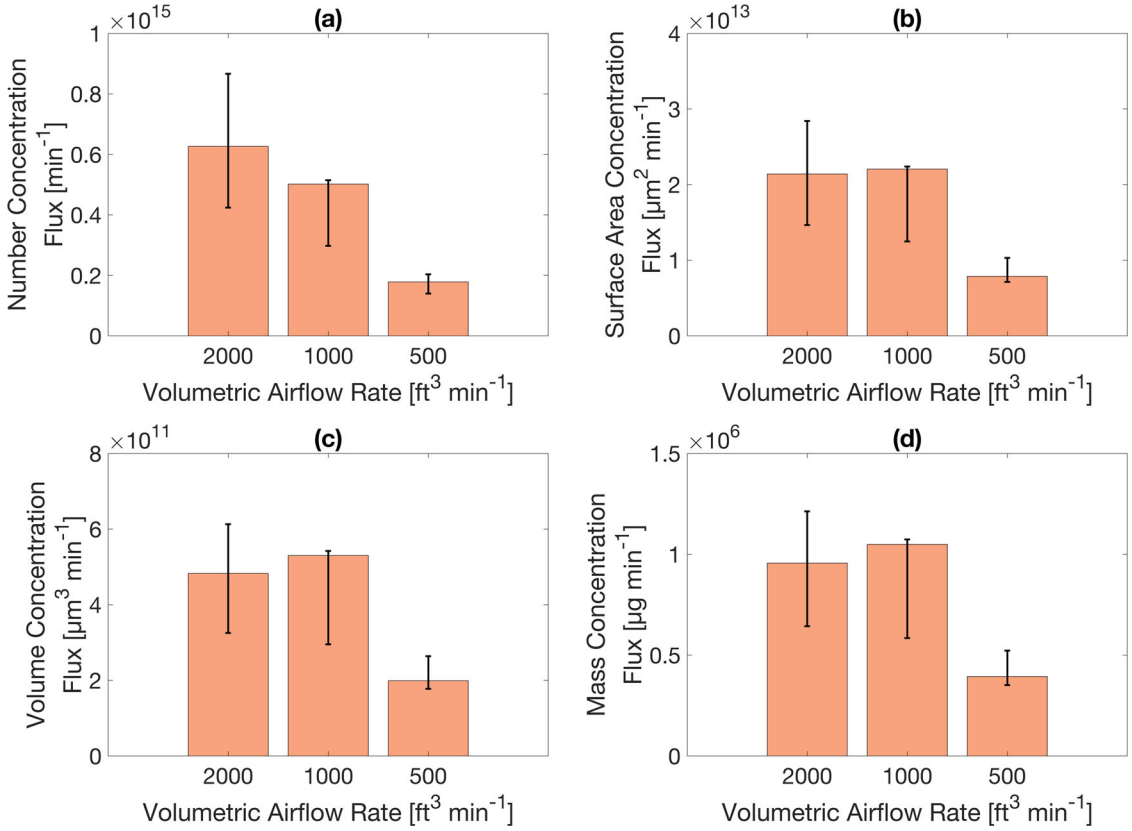

Fig. 13. Size-integrated number, surface area, volume, and mass concentration fluxes in the test rig as determined via SMPS measurements taken upstream of the test filter. Bar heights represent median values, and error bars indicate the IQR (25th–75th percentile). Calculations are integrated across a size range of D_{em} = 20 to 982 nm, using a bulk density of $\rho_p = 1.98\,g\ cm^{-3}$ for mass concentration flux estimates.

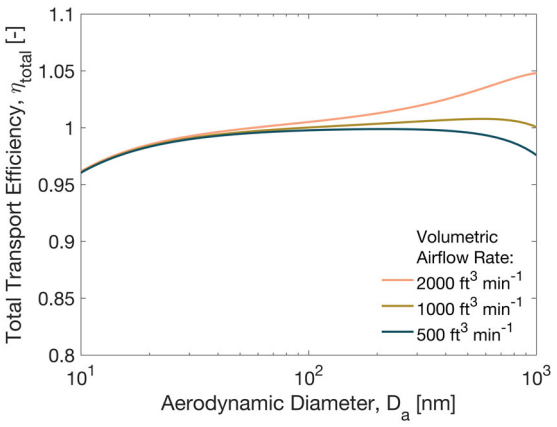

Fig. 14. Theoretical size-resolved total aerosol sample transport efficiencies in the sampling manifold connected to the test rig.

Characterization of in-duct volumetric airflow rates and RH in the HVAC filter test rig

The sensitivity tests required three volumetric airflow rate settings: 500 ft^3 min^{-1}, 1000 ft^3 min^{-1}, and 2000 ft^3 min^{-1}. High stability in volumetric airflow rates was achieved in the test rig across all setpoints. Median volumetric airflow rates for all setpoints complied with ANSI/ASHRAE Standard 52.2 requirements (ASHRAE 2017), maintaining rates within ±2% of the designated setpoints (Supplementary Figure S7). Slightly greater variability was observed at the 500 ft^3 min^{-1} and 1000 ft^3 min^{-1} settings, likely due to increased measurement uncertainty associated with the pitot-tube array at lower air velocities (Folsom 1956; Klopfenstein 1998). The proposed loading procedure requires a stricter RH control range (±2.5%) than the ±10% RH specified in ANSI/ASHRAE Standard 52.2 (ASHRAE 2017), given the significant influence of RH on salt aerosol properties and filter loading curves. Median RH values aligned closely with the setpoints: 27.5 ± 2.5%, 42.5 ± 2.5%, and 57.5 ± 2.5% (Supplementary Figure S8).

Aerosol deposition in the sampling manifold and dilution factor of the double dilutor

Figure 14 shows the size-resolved total aerosol sample transport efficiencies for particles ranging from D_a = 10 to 1000 nm. The sampling system exhibited high transport efficiencies, consistently exceeding 0.95 across the TAG-generated submicrometer KCl aerosol size range, indicating minimal particle loss. For particles larger than D_a = 100 nm, transport efficiencies slightly exceeded 1 at volumetric airflow rates of 1000 and 2000 ft^3 min^{-1}, likely due to sub-isokinetic sampling caused by the in-duct air velocity surpassing the sampling air velocity, enhancing the capture of larger particles. This observation underscores the robustness of the sampling system for preserving TAG-generated KCl aerosol characteristics during measurement.

The dilution factor of the double dilutor system positioned upstream of the SMPS and HR-ELPI+ was experimentally verified. A CPC measured particle number concentrations before and after dilution, yielding an observed dilution factor of 65.6, which closely matches the nominal value of 66.9 for the two ejector dilutors arranged in series. This dilution effectively reduced the sample aerosol number concentrations to ranges suitable for measurement with the SMPS and HR-ELPI+. Both the total aerosol transport efficiencies and dilution factors were incorporated into the data analysis and PSD calculations (Equation 2), ensuring an accurate representation of the TAG-generated KCl aerosol characteristics.

Conclusions

This study evaluated the integration of a TAG into a full-scale HVAC filter test rig to generate synthetic submicrometer KCl aerosol for controlled filter loading experiments. The TAG reliably produced stable and reproducible PSDs that closely resemble urban aerosol characteristics under controlled laboratory conditions. Experiments conducted across varying operational conditions, including volumetric airflow rate, salt stick feed rate, and RH, demonstrated the TAG's robustness in simulating realistic urban aerosol loading scenarios. The results highlight the TAG's capability to replicate the Aitken and accumulation modes of urban aerosol number and mass PSDs, while acknowledging challenges in reproducing multimodal distributions and coarse-mode particles typical of urban environments. This methodology represents a significant advancement in standardized testing of HVAC filter loading, bridging the gap between laboratory experiments and real-world performance evaluations. By enabling realistic and rapid HVAC filter aging studies, this approach supports the development and optimization of advanced HVAC filters to improve indoor air quality, energy efficiency, and system reliability. Future research efforts could focus on developing multimodal aerosol generation systems that incorporate both organic and inorganic components, further aligning laboratory-generated aerosol with real-world urban conditions, such as combining TAG-generated submicrometer aerosol with different loading dusts. In addition, the electrostatic charge of the KCl aerosol warrants further investigation, and the development of effective neutralization techniques may help minimize charging effects and improve test repeatability.

Acknowledgments

The authors are grateful for the support of the ASHRAE RP-1734 Project Monitoring Subcommittee: Paolo Tronville, Geoff Crosby, Bruce McDonald, Tom Justice, and Brian Krafthefer. The authors are grateful for the support of Nusrat Jung, Ayesha Shah, David Rater, Hajin Park, Iane Loise Moreira Gomes, Laura Ajala, Brian H. Magnuson, Ekpeme Gbemiye-Etta, Caio K. Sugane Hamada, Susan L. Huster, Elliot P. Cram, and Ta-Kuan Chuang.

Disclosure statement

No potential conflict of interest was reported by the author(s).

Funding

This work was supported by the American Society of Heating, Refrigerating, and Air-Conditioning Engineers (ASHRAE) under Grant RP-1734.

ORCID

Chunxu Huang http://orcid.org/0009-0009-1608-496X
Brandon E. Boor http://orcid.org/0000-0003-1011-4100

References

Alavy M, Li T, Siegel JA. 2020. Energy use in residential buildings: analyses of high-efficiency filters and HVAC fans. Energy Build. 209:109697. https://doi.org/10.1016/j.enbuild.2019.109697

Alavy M, Siegel JA. 2019. IAQ and energy implications of high efficiency filters in residential buildings: a review (RP-1649). Sci Technol Built Environ. 25(3):261–271. https://doi.org/10.1080/23744731.2018.1526012

Arunkumar R et al. 2007. High-efficiency particulate air filter test stand and aerosol generator for particle loading studies. Rev Sci Instrum. 78(8):085105. https://doi.org/10.1063/1.2771421

ASHRAE. 2017. Method of testing general ventilation air-cleaning devices for removal efficiency by particle size. ASHRAE Standard 52.2-2017. American Society of Heating, Refrigerating, and Air-Conditioning Engineers.

Berry G, Beckman I, Cho H. 2023. A comprehensive review of particle loading models of fibrous air filters. J Aerosol Sci. 167:106078. https://doi.org/10.1016/j.jaerosci.2022.106078

Biskos G, Vons V, Yurteri CU, Schmidt-Ott A. 2008. Generation and sizing of particles for aerosol-based nanotechnology. KONA. 26(0):13–35. https://doi.org/10.14356/kona.26.2008006

Brook RD et al. 2010. Particulate matter air pollution and cardiovascular disease: an update to the scientific statement from the American Heart Association. Circulation. 121(21):2331–2378. https://doi.org/10.1161/CIR.0b013e3181dbece1

Chen P et al. 2019. Preparation of polyacrylate hollow microspheres via facile spray drying. Appl Sci. 9(2):228. https://doi.org/10.3390/app9020228

Cummings BE, Li Y, DeCarlo PF, Shiraiwa M, Waring MS. 2020. Indoor aerosol water content and phase state in U.S. residences: impacts of relative humidity, aerosol mass and composition, and mechanical system operation. Environ Sci Process Impacts. 22(10):2031–2057. https://doi.org/10.1039/d0em00122h

Deng Z, Dong B, Guo X, Zhang J. 2024. Impact of indoor air quality and multi-domain factors on human productivity and physiological responses: a comprehensive review. Indoor Air. 2024(1): e5584960. https://doi.org/10.1155/2024/5584960

Endo Y, Chen DR, Pui DYH. 1998a. Bimodal aerosol loading and dust cake formation on air filters. Filtr Sep. 35(2):191–195. https://doi.org/10.1016/S0015-1882(98)91369-6

Endo Y, Chen DR, Pui DYH. 1998b. Effects of particle polydispersity and shape factor during dust cake loading on air filters. Powder Technol. 98(3):241–249. https://doi.org/10.1016/S0032-5910(98)00063-1

Fialkov AB, Yermekov S, Kazakstan K. 1997. Investigations on ions in flames. Prog Energy Combust Sci. 23(5-6):399–528. https://doi.org/10.1016/S0360-1285(97)00016-6

First MW, Rudnick SN, Yan X. 1992. Use of alternative liquids in Laskin nozzle generated aerosols for filter testing. Am Ind Hyg Assoc J. 53(4):242–247. https://doi.org/10.1080/15298669291359591

Folsom RG. 1956. Review of the Pitot tube. J Fluids Eng. 78(7):1447–1460. https://doi.org/10.1115/1.4014062

Freney EJ, Martin ST, Buseck PR. 2009. Deliquescence and efflorescence of potassium salts relevant to biomass-burning aerosol particles. Aerosol Sci Technol. 43(8):799–807. https://doi.org/10.1080/02786820902946620

Frenklach M, Mebel AM. 2020. On the mechanism of soot nucleation. Phys Chem Chem Phys. 22(9):5314–5331. https://doi.org/10.1039/d0cp00116c

Giffin PK, Parsons MS, Unz RJ, Waggoner CA. 2012. Large-scale generic test stand for testing multiple configurations of air filters utilizing a range of particle size distributions. Rev Sci Instrum. 83(5):055105. https://doi.org/10.1063/1.4717671

Gupta A, Novick VJ, Biswas P, Monson PR. 1993. Effect of humidity and particle hygroscopicity on the mass loading capacity of high efficiency particulate air (HEPA) filters. Aerosol Sci Technol. 19(1):94–107. https://doi.org/10.1080/02786829308959624

Hanley JT, Ensor DS, Fonde KK, Sparks LE. 1999. The effect of loading dust type on the filtration efficiency of electrostatically charged filters. In: Proceedings of the 8th International Conference on Indoor Air Quality and Climate.

Hanley JT, Ensor DS, Smith DD, Sparks LE. 1994. Fractional aerosol filtration efficiency of in-duct ventilation air cleaners. Indoor Air. 4(3):169–178. https://doi.org/10.1111/j.1600-0668.1994.t01-1-00005.x

Hinds WC, Zhu Y. 2022. Aerosol technology: properties, behavior, and measurement of airborne particles. 3rd ed. John Wiley & Sons, Inc.

Hu D et al. 2010. Hygroscopicity of inorganic aerosols: size and relative humidity effects on the growth factor. Aerosol Air Qual Res. 10(3):255–264. https://doi.org/10.4209/aaqr.2009.12.0076

Hu N, Yuan F, Gram A, Yao R, Sadrizadeh S. 2024. Review of experimental measurements on particle size distribution and airflow behaviors during human respiration. Build Environ. 247: 110994. https://doi.org/10.1016/j.buildenv.2023.110994

Huang C, Jung N, Boor BE. 2025. A novel methodology for rapid aging of HVAC filters using a synthetic submicron aerosol: effects of HVAC system operational and environmental conditions on filter loading. Build Environ. 286:113564. https://doi.org/10.1016/j.buildenv.2025.113564

ISO. 2024. Road vehicles—test contaminants for filter evaluation—part 1: Arizona test dust. 3rd ed. ISO 12103-1:2024. International Organization for Standardization. https://standards.iteh.ai/catalog/standards/iso/16cbf0b5-026b-4063-b616-6a03c18f3906/iso-12103-1-2024

Jiang J, Jung N, Boor BE. 2021a. Using building energy and smart thermostat data to evaluate indoor ultrafine particle source and loss processes in a net-zero energy house. ACS EST Eng. 1(4): 780–793. https://doi.org/10.1021/acsestengg.1c00002

Jiang J et al. 2021b. Ethanol-based disinfectant sprays drive rapid changes in the chemical composition of indoor air in residential buildings. J Hazard Mater Lett. 2:100042. https://doi.org/10.1016/j.hazl.2021.100042

Jiang J et al. 2023. Siloxane emissions and exposures during the use of hair care products in buildings. Environ Sci Technol. 57(48): 19999–20009. https://doi.org/10.1021/acs.est.3c05156

Johansson KO, Head-Gordon MP, Schrader PE, Wilson KR, Michelsen HA. 2018. Resonance-stabilized hydrocarbon-radical chain reactions may explain soot inception and growth. Science. 361(6406):997–1000. https://doi.org/10.1126/science.aat3417

Kamaruzzaman S, Sabrani NA. 2011. The effect of indoor air quality (IAQ) towards occupants' psychological performance in office buildings. J Rekabentuk Dan Binaan. 4:49–61. https://spaj.ukm.my/jsb/index.php/jdb/article/view/40

Kang S, Lai WT, Chen SC, Pui DYH. 2018. Measurement of dispersity of ISO A2 fine dusts by shadowgraph method. Powder Technol. 323:186–194. https://doi.org/10.1016/j.powtec.2017.10.004

Kim SC, Wang J, Shin WG, Scheckman JH, Pui DYH. 2009. Structural properties and filter loading characteristics of soot agglomerates. Aerosol Sci Technol. 43(10):1033–1041. https://doi.org/10.1080/02786820903131081

Klopfenstein R. 1998. Air velocity and flow measurement using a Pitot tube. ISA Trans. 37(4):257–263. https://doi.org/10.1016/s0019-0578(98)00036-6

Knobloch Y et al. 2024. Aerosol collection efficiency enhancement in HVAC systems through electrical field-induced filter media polarization. Sci Technol Built Environ. 30(5):498–509. https://doi.org/10.1080/23744731.2024.2327977

Kulkarni P, Baron PA, Willeke K. 2011. Aerosol measurement: principles, techniques, and applications. 3rd ed. John Wiley & Sons, Inc.

Lee JK, Kim SC, Liu BYH. 2001. Effect of bi-modal aerosol mass loading on the pressure drop for gas cleaning industrial filters. Aerosol Sci Technol. 35(4):805–814. https://doi.org/10.1080/02786201753227352

Lee KS et al. 2020. Dust loading performance of a non-electret HVAC filter module in the presence of an external electric field. Sep Purif Technol. 250:117204. https://doi.org/10.1016/j.seppur.2020.117204

Li Q et al. 2022. Experimental study on the synthetic dust loading characteristics of air filters. Sep Purif Technol. 284:120209. https://doi.org/10.1016/j.seppur.2021.120209

Li T, Siegel J. 2020a. Laboratory performance of new and used residential HVAC filters: comparison to field results (RP-1649). Sci Technol Built Environ. 26(6):844–855. https://doi.org/10.1080/23744731.2020.1738871

Li T, Siegel JA. 2020b. In situ efficiency of filters in residential central HVAC systems. Indoor Air. 30(2):315–325. https://doi.org/10.1111/ina.12633

Liu J et al. 2024. Real-time evaluation of terpene emissions and exposures during the use of scented wax products in residential buildings with PTR-TOF-MS. Build Environ. 255:111314. https://doi.org/10.1016/j.buildenv.2024.111314

Liu J et al. 2025. Indoor nanoparticle emissions and exposures during heat-based hair styling activities. Environ Sci Technol. 59(32):17103–17115. https://doi.org/10.1021/acs.est.4c14384

Ma X et al. 2022. Effect of air flow rate and temperature on the atomization characteristics of biodiesel in internal and external flow fields of the pressure swirl nozzle. Energy. 253:124112. https://doi.org/10.1016/j.energy.2022.124112

McMurry PH, Stolzenburg MR. 1989. On the sensitivity of particle size to relative humidity for Los Angeles aerosols. Atmos Environ. 23(2):497–507. https://doi.org/10.1016/0004-6981(89)90593-3

Morawska L, Buonanno G, Mikszewski A, Stabile L. 2022. The physics of respiratory particle generation, fate in the air, and inhalation. Nat Rev Phys. 4(11):723–734. https://doi.org/10.1038/s42254-022-00506-7

Neo RG, Wu K, Tan SC, Zhou W. 2022. Effect of spray distance and powder feed rate on particle velocity in cold spray processes. Metals. 12(1):75. https://doi.org/10.3390/met12010075

Patra SS et al. 2024a. Dynamics of nanocluster aerosol in the indoor atmosphere during gas cooking. PNAS Nexus. 3(2):pgae044. https://doi.org/10.1093/pnasnexus/pgae044

Patra SS et al. 2024b. Rapid nucleation and growth of indoor atmospheric nanocluster aerosol during the use of scented volatile chemical products in residential buildings. ACS EST Air. 1(10):1276–1293. https://doi.org/10.1021/acsestair.4c00118

Patra SS, Wu T, Wagner DN, Jiang J, Boor BE. 2021. Real-time measurements of fluorescent aerosol particles in a living laboratory office under variable human occupancy and ventilation conditions. Build Environ. 205:108249. https://doi.org/10.1016/j.buildenv.2021.108249

Poon WS, Liu BYH. 1997a. A bimodal loading test for engine and general purpose air cleaning filters. SAE Tech Pap Ser. https://doi.org/10.4271/970674

Poon WS, Liu BYH. 1997b. Dust loading behavior of engine and general purpose air cleaning filters. SAE Tech Pap Ser. https://doi.org/10.4271/970676

Pöschl U. 2005. Atmospheric aerosols: composition, transformation, climate and health effects. Angew Chem Int Ed Engl. 44(46):7520–7540. https://doi.org/10.1002/anie.200501122

Raynor PC, Soo JC. 2003. Dust loading on electrostatically charged filters in a standard test and a real HVAC system. Filt Sep. 40(2):35–39. https://doi.org/10.1016/S0015-1882(03)80068-X

Reponen T, Willeke K, Ulevicius V, Reponen A, Grinshpun SA. 1996. Effect of relative humidity on the aerodynamic diameter and respiratory deposition of fungal spores. Atmos Environ. 30(23):3967–3974. https://doi.org/10.1016/1352-2310(96)00128-8

Rosales CMF et al. 2022. Chemistry and human exposure implications of secondary organic aerosol production from indoor terpene ozonolysis. Sci Adv. 8(8):eabj9156. https://doi.org/10.1126/sciadv.abj9156

Sgro LA, D'Anna A, Minutolo P. 2010. Charge distribution of incipient flame-generated particles. Aerosol Sci Technol. 44(8):651–662. https://doi.org/10.1080/02786826.2010.483701

Stephens B, Novoselac A, Siegel JA. 2010. The effects of filtration on pressure drop and energy consumption in residential HVAC systems (RP-1299). HVAC&R Res. 16(3):273–294. https://doi.org/10.1080/10789669.2010.10390905

Tham KW. 2016. Indoor air quality and its effects on humans—a review of challenges and developments in the last 30 years. Energy Build. 130:637–650. https://doi.org/10.1016/j.enbuild.2016.08.071

Tian X, Ou Q, Liu J, Liang Y, Pui DYH. 2019. Particle loading characteristics of a two-stage filtration system. Sep Purif Technol. 215:351–359. https://doi.org/10.1016/j.seppur.2019.01.033

Tofful L, Canepari S, Sargolini T, Perrino C. 2021. Indoor air quality in a domestic environment: combined contribution of indoor and outdoor PM sources. Build Environ. 202:108050. https://doi.org/10.1016/j.buildenv.2021.108050

Tronville P, Rivers RD. 2005. International standards: filters for vehicular applications. Filt Sep. 42(9):24–27. https://doi.org/10.1016/S0015-1882(05)70692-3

Tumminello PR et al. 2021. Evolution of sea spray aerosol particle phase state across a phytoplankton bloom. ACS Earth Space Chem. 5(11):2995–3007. https://doi.org/10.1021/acsearthspacechem.1c00186

Tumminello PR et al. 2024. Size-dependent nascent sea spray aerosol bounce fractions and estimated viscosity: the role of divalent cation enrichment, surface tension, and the Kelvin effect. Environ Sci Technol. 58(44):19666–19678. https://doi.org/10.1021/acs.est.4c04312

United Nations. 2018. Revision of world urbanization prospects. Department of Economic and Social Affairs. United Nations. https://www.un.org/en/desa/2018-revision-world-urbanization-prospects

Valmari T, Lehtimäki M, Taipale A. 2006. Filter clogging by bimodal aerosol. Aerosol Sci Technol. 40(4):255–260. https://doi.org/10.1080/02786820500543282

Van Tran V, Park D, Lee YC. 2020. Indoor air pollution, related human diseases, and recent trends in the control and improvement of indoor air quality. Int J Environ Res Public Health. 17(8):2927. https://doi.org/10.3390/ijerph17082927

Viswanathan S et al. 2015. Effect of particle size distribution on the deep-bed capture efficiency of an exhaust particulate filter. J Eng Gas Turbines Power. 137(10):102–109. https://doi.org/10.1115/1.4030098

Wang Q, Lin X, Chen DR. 2016. Effect of dust loading rate on the loading characteristics of high efficiency filter media. Powder Technol. 287:20–28. https://doi.org/10.1016/j.powtec.2015.09.032

Wang Y et al. 2017. Influence of flame-generated ions on the simultaneous charging and coagulation of nanoparticles during combustion. Aerosol Sci Technol. 51(7):833–844. https://doi.org/10.1080/02786826.2017.1304635

Weingartner E, Baltensperger U, Burtscher H. 1995. Growth and structural change of combustion aerosols at high relative humidity. Environ Sci Technol. 29(12):2982–2986. https://doi.org/10.1021/es00012a014

Wise ME et al. 2007. Hygroscopic behavior of NaCl-bearing natural aerosol particles using environmental transmission electron microscopy. J Geophys Res. 112:D10224. https://doi.org/10.1029/2006JD007678

Wu T, Boor BE. 2020. Characterization of a thermal aerosol generator for HVAC filtration experiments (RP-1734). Sci Technol Built Environ. 26(6):816–834. https://doi.org/10.1080/23744731.2020.1730661

Wu T, Boor BE. 2021. Urban aerosol size distributions: a global perspective. Atmos Chem Phys. 21(11):8883–8914. https://doi.org/10.5194/acp-21-8883-2021

Wu T et al. 2024. Modern buildings act as a dynamic source and sink for urban air pollutants. Cell Rep Sustain. 1(5):100103. https://doi.org/10.1016/j.crsus.2024.100103

Zaatari M, Novoselac A, Siegel J. 2014. The relationship between filter pressure drop, indoor air quality, and energy consumption in rooftop HVAC units. Build Environ. 73:151–161. https://doi.org/10.1016/j.buildenv.2013.12.010

Zhang Z, Jiang F. 2016. In-place HEPA filter testing by the sodium flame method. Powder Technol. 301:615–621. https://doi.org/10.1016/j.powtec.2016.06.046